

# Linking ice and gas in the Coronet cluster in Corona Australis

G. Perotti<sup>1,2</sup>, J. K. Jørgensen<sup>1</sup>, W. R. M. Rocha<sup>3</sup>, A. Plunkett<sup>4</sup>, E. Artur de la Villarmois<sup>5,6</sup>, L. E. Kristensen<sup>1</sup>,  
M. Sewilo<sup>7,8,9</sup>, P. Bjerkeli<sup>10</sup>, H. J. Fraser<sup>11</sup>, and S. B. Charnley<sup>12</sup>

<sup>1</sup> Niels Bohr Institute, University of Copenhagen, Øster Voldgade 5–7, 1350 Copenhagen K, Denmark

<sup>2</sup> Max Planck Institute for Astronomy, Königstuhl 17, D-69117 Heidelberg, Germany  
e-mail: perotti@mpia.de

<sup>3</sup> Laboratory for Astrophysics, Leiden Observatory, Leiden University, PO Box 9513, 2300 RA Leiden, The Netherlands

<sup>4</sup> National Radio Astronomy Observatory, 520 Edgemont Rd, Charlottesville, VA 22903-2475, USA

<sup>5</sup> Instituto de Astrofísica, Ponticia Universidad Católica de Chile, Av. Vicuña Mackenna 4860, 7820436 Macul, Santiago, Chile

<sup>6</sup> Núcleo Milenio de Formación Planetaria (NPF), Chile

<sup>7</sup> Exoplanets and Stellar Astrophysics Laboratory, NASA Goddard Space Flight Center, Greenbelt, MD 20771, USA

<sup>8</sup> Department of Astronomy, University of Maryland, College Park, MD 20742, USA

<sup>9</sup> Center for Research and Exploration in Space Science and Technology, NASA Goddard Space Flight Center, Greenbelt, MD 20771, USA

<sup>10</sup> Department of Space, Earth, and Environment, Chalmers University of Technology, Onsala Space Observatory, 439 92 Onsala, Sweden

<sup>11</sup> School of Physical Sciences, The Open University, Walton Hall, Milton Keynes, MK7 6AA, United Kingdom

<sup>12</sup> Astrochemistry Laboratory, NASA Goddard Space Flight Center, Greenbelt, MD 20771, USA

Received ; accepted

## ABSTRACT

*Context.* During the journey from the cloud to the disc, the chemical composition of the protostellar envelope material can be either preserved or processed to varying degrees depending on the surrounding physical environment.

*Aims.* This work aims to constrain the interplay of solid (ice) and gaseous methanol (CH<sub>3</sub>OH) in the outer regions of protostellar envelopes located in the Coronet cluster in Corona Australis (CrA), and assess the importance of irradiation by the Herbig Ae/Be star R CrA. CH<sub>3</sub>OH is a prime test-case as it predominantly forms as a consequence of the solid-gas interplay (hydrogenation of condensed CO molecules onto the grain surfaces) and it plays an important role in future complex molecular processing.

*Methods.* We present 1.3 mm Submillimeter Array (SMA) and Atacama Pathfinder Experiment (APEX) observations towards the envelopes of four low-mass protostars in the Coronet. Eighteen molecular transitions of seven species are identified. We calculate CH<sub>3</sub>OH gas-to-ice ratios in this strongly irradiated cluster and compare them with ratios determined towards protostars located in less irradiated regions such as the Serpens SVS 4 cluster in Serpens Main and the Barnard 35A cloud in the  $\lambda$  Orionis region.

*Results.* The CH<sub>3</sub>OH gas-to-ice ratios in the Coronet vary by one order of magnitude (from  $1.2 \times 10^{-4}$  to  $3.1 \times 10^{-3}$ ) which is similar to less irradiated regions as found in previous studies. We find that the CH<sub>3</sub>OH gas-to-ice ratios estimated in these three regions are remarkably similar despite the different UV radiation field intensities and formation histories.

*Conclusions.* This result suggests that the overall CH<sub>3</sub>OH chemistry in the outer regions of low-mass envelopes is relatively independent of variations in the physical conditions and hence that it is set during the prestellar stage.

**Key words.** ISM: molecules — stars:protostars — astrochemistry — molecular processes — ISM:individual objects: R CrA

## 1. Introduction

Solar-type stars and planets form inside molecular clouds, when dense cores undergo gravitational collapse. While collapsing, the gas and dust constituting the clouds is assembled into infalling envelopes, streamers and circumstellar discs, which supply the fundamental ingredients for planet formation (see e.g., Pineda et al. 2023). Recent observations (e.g., Andrews et al. 2018; Harsono et al. 2018; Keppler et al. 2018; Segura-Cox et al. 2020) suggest that planets form earlier than previously thought (a few  $10^5$  years; Tychoniec et al. 2020) and in tandem with their host stars (Alves et al. 2020). In this context, it is still un-

clear whether the composition of the molecular cloud material is preserved when becoming part of planets or, instead, entirely thermally processed losing the natal cloud's chemical fingerprint (see e.g., Jørgensen et al. 2020; van Dishoeck & Bergin 2020 for recent reviews).

To address this query it is necessary to study how the environment impacts the physical and chemical properties of embedded protostars and their discs. For instance, external irradiation (Winter et al. 2020) and cosmic ray ionization (Kuffmeier et al. 2020) might shape the chemical and physical evolution of forming low-mass stars by e.g., photoevaporating their discs (van Terwisga et al. 2020; Ha-

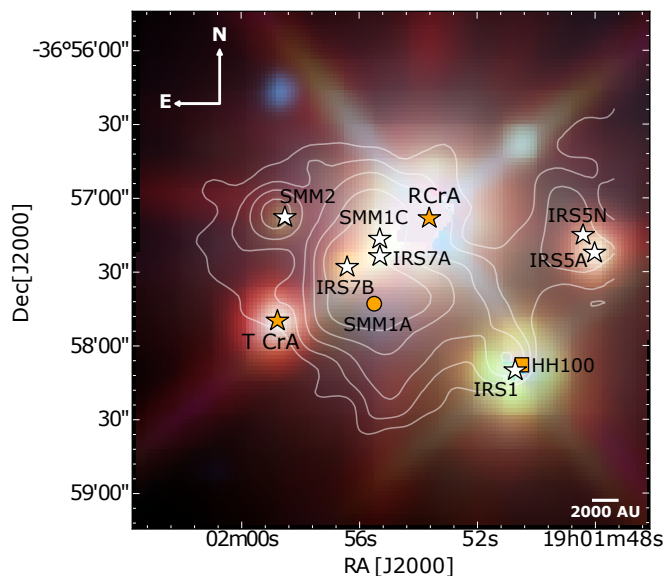


Fig. 1: Three-color image of the Coronet cluster (*WISE* 3.4  $\mu\text{m}$  (blue), 4.6  $\mu\text{m}$  (green), and 12  $\mu\text{m}$  (red) bands; Wright et al. 2010) overlaid with SCUBA 850  $\mu\text{m}$  density flux Nutter et al. (2005); contours are in decreasing steps starting at the peak flux (3.7 Jy beam $^{-1}$ ) and subtracting 30% from the previous level. The white stars mark the positions of Class 0/I YSOs in the R CrA/Coronet region (Peterson et al. 2011; Nutter et al. 2005), whereas the orange stars indicate the Herbig Ae/Be star R CrA and the T Tauri star T CrA. The pre-stellar core candidate SMM1A is indicated with an orange circle and the orange square represents the Herbig Haro object HH100.

worth et al. 2021 and references therein) or leading to less massive discs (Cazzoletti et al. 2019). In this paper we investigate the variations of the methanol gas and ice towards deeply embedded sources in Corona Australis, to study the effects of external irradiation on the gas-to-ice ratios.

CH<sub>3</sub>OH is the most suitable molecule for the main aim of this work because it is abundantly detected in both solid and gas phases (Boogert et al. 2015; McGuire 2022). Most importantly, it is primarily formed in the solid-state (Watanabe & Kouchi 2002; Fuchs et al. 2009; Qasim et al. 2018; Simons et al. 2020; Santos et al. 2022) as its gas-phase formation pathways are considerably less efficient (Roberts & Millar 2000; Garrod & Herbst 2006; Geppert et al. 2006). Finally, CH<sub>3</sub>OH is regarded as the gateway species for the formation of complex organic molecules both in the solid-state (e.g., Öberg et al. 2009b; Chuang et al. 2016; Fedoseev et al. 2017) and in the gas phase (e.g., Shannon et al. 2014; Balucani et al. 2015).

Corona Australis (CrA) is one of the nearest regions with ongoing star-formation, located at a distance of  $149.4 \pm 0.4$  pc as estimated from *Gaia*-DR2 measurements (Galli et al. 2020). The most recent census of the cloud counts 393 young stellar object (YSO) candidates (Esplin & Luhman 2022): these are relatively evolved, mainly Class II and III sources, and they are predominantly concentrated in the most extincted region, the "head" (Peterson et al. 2011; Alves et al. 2014). The correlation between the star formation activity and the head-tail structure of Corona

Australis has been investigated by Dib & Henning (2019), who found that the spatial distribution of dense cores is a consequence of the physical conditions of the large scale environment present at the time the cloud assembled. The youngest population of YSOs (Class 0/I) is situated in the Coronet cluster (Taylor & Storey 1984; Forbrich et al. 2007; Forbrich & Preibisch 2007), also associated with the luminous Herbig Ae/Be star R CrA (Peterson et al. 2011).

Figure 1 displays a section of the Coronet cluster and a summary of the principal cluster members is provided in Table 1. The Herbig Ae/Be R CrA (spectral type B5–B8; Gray et al. 2006; Bibo et al. 1992) is the brightest star in this very young cluster that has an estimated age of 0.5–1 Myr (Sicilia-Aguilar et al. 2011). Due to the variable nature of R CrA, its stellar mass and luminosity are uncertain (Mesa et al. 2019). Recent *Very Large Telescope* (VLT)/SPHERE observations of R CrA resolved a companion at a separation of  $\sim 0.156''$ – $0.184''$  and complex extended jet-like structures around the star (Mesa et al. 2019). A second variable star, the T Tauri star T CrA is present in the Coronet cluster, approximately  $30''$  to the south-east of R CrA (Herbig 1960; Taylor & Storey 1984). The region surrounding the two variable stars harbours seven identified Class 0/I YSOs (Table 1).

The Coronet cluster members have been at the center of active multi-wavelength research, mostly aimed at the characterization of the properties of YSOs at very early stages of stellar evolution. Some of the most studied objects are IRS7B, IRS7A, SMM1A, SMM1C and SMM2 (Nutter et al. 2005; Groppi et al. 2007; Miettinen et al. 2008; Chen & Arce 2010; Peterson et al. 2011). The spectral energy distributions (SEDs) of the cluster members have been investigated by Groppi et al. (2007), suggesting that SMM1C is a Class 0 YSO and IRS7B is a transitional Class 0/I object. IRS7A and SMM2 are likely Class I sources (Peterson et al. 2011) and SMM1A is classified as a pre-stellar core candidate (Nutter et al. 2005; Chen & Arce 2010). IRS1, IRS5N and IRS5A are suggested as Class I YSO based on submillimeter and infrared observations (Peterson et al. 2011).

Along with the identification and the evolutionary stage designation of the YSOs in the Coronet, their chemical evolution has been the subject of a large number of studies over the last decades. The line-rich spectra of IRS7B and IRS7A have been investigated with the *Atacama Pathfinder EXperiment* (APEX) single-dish telescope by Schöier et al. (2006), who reported different kinetic temperatures for formaldehyde (H<sub>2</sub>CO) and methanol (>30 K for H<sub>2</sub>CO and  $\approx 20$  K for CH<sub>3</sub>OH). Lindberg & Jørgensen (2012) suggested that the high temperatures in the region (>30 K) traced by the emission of H<sub>2</sub>CO, are caused by external irradiation from the Herbig Ae/Be star R CrA. With the purpose of analyzing the impact of external irradiation on the molecular inventory of low-mass protostars, systematic unbiased line surveys have been carried out firstly towards IRS7B with the *Atacama Submillimeter Telescope Experiment* (ASTE) by Watanabe et al. (2012), and extended to other Coronet cluster members using APEX by Lindberg et al. (2015). These systematic surveys confirmed that external irradiation can affect the chemical nature of protostars, particularly by enhancing the abundances of Photon-Dominated Regions (PDRs) tracers (such as CN, C<sub>2</sub>H, and c-C<sub>3</sub>H<sub>2</sub>). High-resolution *Atacama Large Millimeter/submillimeter Array* (ALMA) observations found a low column density of CH<sub>3</sub>OH in the inner hot regions

Table 1: Overview of the Coronet cluster objects.

| Object     | RA<br>[J2000] | DEC<br>[J2000] | Designation <sup>(a)</sup> | Other names <sup>(b)</sup> |
|------------|---------------|----------------|----------------------------|----------------------------|
| IRS5A      | 19:01:48.03   | -36:57:22.2    | Class I YSO                | CrA-19                     |
| IRS5N      | 19:01:48.46   | -36:57:14.7    | Class I YSO                | CrA-20                     |
| HH100 IRS1 | 19:01:50.56   | -36:58:08.9    | Herbig-Haro object         | –                          |
| IRS1       | 19:01:50.68   | -36:58:09.7    | Class I YSO                | VSt 15, TS 2.6             |
| R CrA      | 19:01:53.67   | -36:57:08.0    | Herbig Ae/Be star          | –                          |
| SMM1C      | 19:01:55.29   | -36:57:17.0    | Class I YSO                | B9, Brown 9                |
| IRS7A      | 19:01:55.32   | -36:57:21.9    | Class I YSO                | IRS7W, IRS7                |
| SMM1A      | 19:01:55.60   | -36:57:43.0    | Pre-stellar core           | –                          |
| IRS7B      | 19:01:56.40   | -36:57:28.3    | Class I YSO                | SMM1B, IRS7E               |
| SMM2       | 19:01:58.54   | -36:57:08.5    | Class I YSO                | CrA-43, WMB55              |
| T CrA      | 19:01:58.78   | -36:57:49.9    | T Tauri star               | –                          |

**Notes.** All the coordinates are taken from Peterson et al. (2011), except for SMM1A which comes from Nutter et al. (2005) and HH100 IRS1 from Boogert et al. (2008). <sup>(a)</sup> The YSO class is assigned from the spectral index  $\alpha$  reported in Peterson et al. (2011); the objects designated as "Class I YSO" are Class I or younger. <sup>(b)</sup> From Peterson et al. (2011) and Lindberg & Jørgensen (2012).

of the protostellar envelopes which could either be due to the suppressed CH<sub>3</sub>OH formation in ices at the higher temperatures in the region or due to the envelope structures on small scales being affected by the presence of a disc (Lindberg et al. 2014). The latter interpretation is supported by recent observations (Artur de la Villarmois et al. 2018; van Gelder et al. 2022) and models (Nazari et al. 2022b).

Along with the gas-phase molecular species, the composition of interstellar ices towards a few objects in the Coronet cluster (IRS5A, IRS5B, HH100 IRS1, IRS7A, IRS7B) has been modelled (Siebenmorgen & Gredel 1997) and investigated in the near-infrared (3–5  $\mu$ m) with the *Very Large Telescope* (Pontoppidan et al. 2003), in the mid-infrared (5–8  $\mu$ m) using the *Infrared Space Observatory* (Keane et al. 2001) and as part of the *Spitzer* Space Telescope c2d Legacy Program (5–8  $\mu$ m by Boogert et al. 2008; 8–10  $\mu$ m by Bottinelli et al. 2010, and 14.5–16.5  $\mu$ m by Pontoppidan et al. 2008). Ice features attributed to H<sub>2</sub>O, CO, CO<sub>2</sub>, NH<sub>3</sub>, CH<sub>3</sub>OH were securely identified in the astronomical spectra of the targeted sources.

This paper explores the variations of CH<sub>3</sub>OH gas and ice abundances, investigating the effects of external irradiation on the gas-phase and solid-state chemistries of the youngest objects in the Coronet cluster. We present *Submillimeter Array* (SMA) observations towards five Coronet cluster members, thus complementing previous observations at 1.3 mm (Lindberg & Jørgensen 2012) by increasing the number of detected chemical species in this region. To probe the CH<sub>3</sub>OH large-scale emission, an APEX 150''  $\times$  150'' map of the CH<sub>3</sub>OH  $J_K = 5_K - 4_K$  Q-branch is also presented. The column densities of H<sub>2</sub>O and CH<sub>3</sub>OH ice are taken from Boogert et al. (2008). Furthermore, the dependence of gas-to-ice ratios on the physical conditions are addressed, by determining gas-to-ice ratios of CH<sub>3</sub>OH in this strongly irradiated cluster and comparing them with ratios obtained towards less irradiated star-forming regions (Perotti et al. 2020, 2021).

The paper is laid out as follows. Section 2 describes both the SMA and APEX observational setups, and the data reduction strategy. In Section 3, we present our key observational results, while the variations on the ice and gas abundance are analysed in Section 4. Section 5 discusses the determined CH<sub>3</sub>OH gas-to-ice ratios and Section 6 summarises our conclusions and lists avenues for future studies.

## 2. Observations

The Coronet cluster was observed with the SMA (Ho et al. 2004) on February 25, 2020, April 28, 30, and May 19, 31, 2021 in the compact configuration, resulting in projected baselines between 17–72 m. The region was covered by one pointing centered on IRS7B with coordinates  $\alpha_{J2000} = 19^{\text{h}}01^{\text{m}}56^{\text{s}}.40$ ,  $\delta_{J2000} = -36^{\circ}57'27''00$  (Fig. 2). The SWARM correlator provided a total frequency coverage of 36 GHz, with the lower sideband covering frequencies from 210.3 to 228.3 GHz and upper sideband from 230.3 to 248.3 GHz. The spectral resolution was 0.6 MHz corresponding to 0.7 km s<sup>-1</sup>.

Data calibration and imaging were performed with the CASA v. 5.7.2 package<sup>1</sup> (McMullin et al. 2007; Bean et al. 2022). The complex gains were calibrated through observations of the quasars 1924-292 and 1957-387 and the bandpass through observations of the bright quasar 3C279. The overall flux calibration was carried out through observations of Vesta and Callisto. Imaging was done using the `tclean` algorithm and a Briggs weighting with a robust parameter of 0.5. The typical synthesised beam size of the SMA data set was 4''.9  $\times$  2''.6 (400 – 700 AU). The position angle (PA) for CH<sub>3</sub>OH, our main molecule of interest, at 241.791 GHz was -8.2°. The PA varies of  $\approx$  4.5° across the covered frequencies.

<sup>1</sup> <http://casa.nrao.edu/>

Table 2: Identified methanol transitions in the SMA and APEX data sets.

| Species            | Transition                                     | Frequency <sup>(a)</sup><br>[GHz] | $A_{ul}^{(a)}$<br>[s <sup>-1</sup> ] | $g_u^{(a)}$ | $E_u^{(a)}$<br>[K] | $n_{cr}^{(b)}$<br>[cm <sup>-3</sup> ] |
|--------------------|--|-----------------------------------|--------------------------------------|-------------|--------------------|---------------------------------------|
| CH <sub>3</sub> OH | 5 <sub>+0</sub> – 4 <sub>+0</sub> E            | 241.700                           | $6.04 \times 10^{-5}$                | 11          | 47.9               | $1.7 \times 10^6$                     |
|                    | 5 <sub>-1</sub> – 4 <sub>-1</sub> E            | 241.767                           | $5.81 \times 10^{-5}$                | 11          | 40.4               | $4.8 \times 10^7$                     |
|                    | 5 <sub>0</sub> – 4 <sub>0</sub> A <sup>+</sup> | 241.791                           | $6.05 \times 10^{-5}$                | 11          | 34.8               | $4.7 \times 10^5$                     |
|                    | 5 <sub>+1</sub> – 4 <sub>+1</sub> E            | 241.879                           | $5.96 \times 10^{-5}$                | 11          | 55.9               | $1.5 \times 10^7$                     |
|                    | 5 <sub>-2</sub> – 4 <sub>-2</sub> E            | 241.904                           | $5.09 \times 10^{-5}$                | 11          | 60.7               | $2.3 \times 10^8$                     |

**Notes.** <sup>(a)</sup> The spectroscopic data are from [Xu et al. \(2008\)](#). They were taken from the Cologne Database for Molecular Spectroscopy (CDMS; [Müller et al. 2001, 2005](#); [Endres et al. 2016](#)) and the Jet Propulsion Laboratory catalog ([Pickett et al. 1998](#)). <sup>(b)</sup> Calculated using a collisional temperature of 30 K and collisional rates from [Rabli & Flower \(2010\)](#). The latter were taken from the Leiden Atomic and Molecular Database (LAMDA; [Schöier et al. 2005](#)).

Additional information on the CH<sub>3</sub>OH large-scale emission towards the Coronet cluster was provided by observations with APEX ([Güsten et al. 2006](#)) during the nights of October 25 – November 4, 2020. The pointing was the same as reported for the SMA observations. The achieved map size is 150'' × 150'', fully covering the region observed by the SMA. The frequencies probed by the APEX observations are in the range 235.1 – 243 GHz, corresponding to the SMA upper side band observations, with a frequency resolution of 0.061 MHz (0.076 km s<sup>-1</sup>). The resulting beam-size of the observations is 27.4'' for CH<sub>3</sub>OH. Data reduction was carried out with the GILDAS package CLASS<sup>2</sup>. Subsequently, the reduced APEX and SMA datasets were combined in CASA v. 5.7.2 using the feathering technique, following the procedure presented in Appendix B.1. of [Perotti et al. \(2020\)](#). The combination of SMA and APEX short-spacing data resulted in mapping the outer regions of protostellar envelopes in the Coronet cluster on scales from ~ 400 – 10 000 AU.

### 3. Results

Figure 2 displays the region targeted by the SMA and APEX observations. The positions of the SMA 1.3 mm continuum peaks coincides with the location of the young stellar objects in the Coronet cluster. The strongest emission is observed towards the two Class 0 sources SMM1C and IRS7B and the Class I objects SMM2 and IRS7A. Fainter emission north of the pre-stellar core candidate SMM1A ([Chen & Arce 2010](#)) is also seen. Apart from the continuum, line emission of seven species was identified (Table A.1). These results are presented and discussed in Appendix A (Figures A.1–A.3). In the remainder of this section we will uniquely focus on the observed methanol (CH<sub>3</sub>OH) emission, our molecule of interest.

Amongst the molecular species detected in the Coronet, methanol is the most suited for the main aim of this work: assessing the effect of external irradiation on the gas-phase and solid-state (ice) chemistries in the outer regions of protostellar envelopes. These are the regions

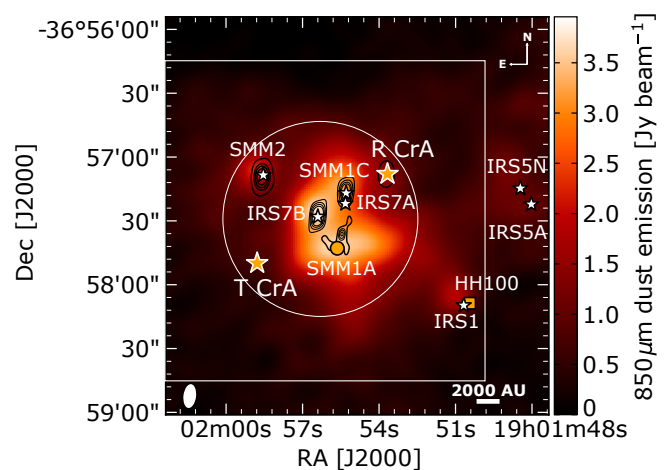


Fig. 2: SMA continuum at 1.3 mm (contours) overlaid with SCUBA 850  $\mu$ m density flux from [Nutter et al. \(2005\)](#). The contours start at  $5\sigma$  and continue in steps of  $5\sigma$  ( $\sigma = 18$  mJy beam<sup>-1</sup>). The empty circle indicates the size of the SMA primary beam, whereas the SMA synthesised beam is shown with a white ellipse in the bottom left corner. The empty rectangle shows the map covered by APEX observations. The stars mark the position of the objects located in the Coronet cluster; refer to Table 1 for their identification.

probed in the presented SMA and APEX observations, at radii  $r > 400$  AU from the protostar. Here, gas-phase methanol is not thermally desorbed and it is a tracer of energetic input such as outflows releasing frozen CH<sub>3</sub>OH to the gas phase (e.g., [Tychoniec et al. 2021](#)). The latter is due to the fact that the most efficient methanol formation pathway in star-forming regions ( $A_V > 9$  mag) occurs on ice-coated dust grains ([Watanabe & Kouchi 2002](#); [Fuchs et al. 2009](#); [Simons et al. 2020](#); [Santos et al. 2022](#)). Consequently, the observed non-thermal CH<sub>3</sub>OH emission in the outer regions of protostellar envelopes does not trace the bulk of the ices, and instead, it probes a fraction of CH<sub>3</sub>OH ice sputtered in outflows or photodesorbed (see [Kristensen](#)

<sup>2</sup> <http://www.iram.fr/IRAMFR/GILDAS>

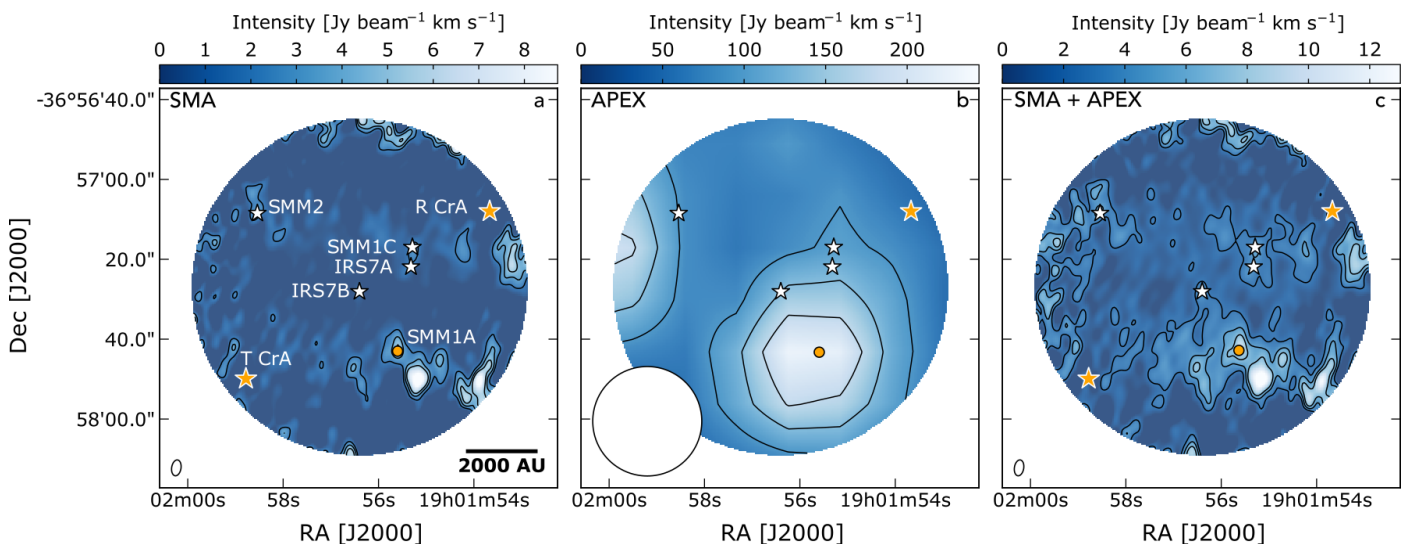


Fig. 3: Primary beam corrected integrated intensity maps for  $\text{CH}_3\text{OH } J = 5_0 - 4_0 \text{ A}^+$  transition ( $E_u = 34.8 \text{ K}$ ) at  $241.791 \text{ GHz}$  detected by the SMA (a), by the APEX telescope (b), and in the combined interferometric SMA and single-dish APEX data (c). All lines are integrated between  $6$  and  $12.5 \text{ km s}^{-1}$ . Contours start at  $5\sigma$  ( $\sigma_{\text{SMA}} = 0.16 \text{ Jy beam}^{-1} \text{ km s}^{-1}$ ,  $\sigma_{\text{APEX}} = 2 \text{ Jy beam}^{-1} \text{ km s}^{-1}$ ,  $\sigma_{\text{SMA+APEX}} = 0.17 \text{ Jy beam}^{-1} \text{ km s}^{-1}$ ) and follow in steps of  $5\sigma$ . The circular field-of-view corresponds to the primary beam of the SMA observations. The synthesised beams are displayed in white in the bottom left corner of each panel.

et al. 2010 for an observational overview of  $\text{CH}_3\text{OH}$  non-thermal desorption processes).

Figure 3 presents primary beam corrected integrated intensity (moment 0) maps of the  $\text{CH}_3\text{OH } J = 5_0 - 4_0 \text{ A}^+$  line for the SMA, APEX, and the combination of interferometric and single-dish data (SMA+APEX). The combined moment 0 maps of the other  $\text{CH}_3\text{OH}$  transitions belonging to the  $J = 5_K - 4_K$  Q-branch are displayed in Appendix A (Figure A.2). We specifically targeted this branch because its multiple transitions are conveniently observable in a narrow spectral range ( $0.2 \text{ GHz}$ ; Table 2) and they are associated to  $E_u$  from  $34.8$  to  $60.7 \text{ K}$ , well below the typical  $\text{CH}_3\text{OH}$  sublimation temperature as inferred from both observations and laboratory experiments ( $70 - 130 \text{ K}$ ; e.g., Kristensen et al. 2010; Penteado et al. 2017). The latter condition has to be satisfied in order to investigate methanol non-thermal desorption processes. Additionally, observations of  $\text{CH}_3\text{OH } J = 5_K - 4_K$  Q-branch make it possible to directly compare our results with previous work on  $\text{CH}_3\text{OH}$  gas-to-ice ratios in nearby star-forming regions using the same facilities, observational strategy, and spectral setups (Perotti et al. 2020, 2021).

By looking at the SMA moment 0 map (Figure 3; panel a) it is clear that the interferometric observations do not sufficiently recover the spatially extended emission originating from the Coronet cluster. In contrast, they filter out  $\approx 90\%$  of the extended emission detected in the APEX data. Unlike for the other species detected in the SMA data, we here want to perform a quantitative analysis of the  $\text{CH}_3\text{OH}$  emission therefore, we combine the SMA data with the APEX map to avoid underestimating the  $\text{CH}_3\text{OH}$  column densities by up to one order of magnitude.

Similarly to the  $\text{CH}_3\text{OH } J = 4_2 - 3_1 \text{ E}$  transition (Fig. A.2; panel g), the  $\text{CH}_3\text{OH } J = 5_0 - 4_0 \text{ A}^+$  emission is tracing the condensations associated to the prestellar core candidate SMM1A. The emission is extended in the APEX

map (Fig. 3; panel b), and confined to two main regions, around SMM1A and to the east of SMM2. The peak intensity is observed also in this case in the vicinity of SMM1A. The same pattern is visible in the SMA + APEX moment 0 map (Fig. 3; panel c), but some  $\text{CH}_3\text{OH}$  emission is also present at the SMM2, IRS7A, and IRS7B source positions although approximately a factor of 4 fainter compared to the peak position.

The  $\text{CH}_3\text{OH}$  column densities towards the Coronet cluster members were determined from the integrated line intensities of the feathered SMA + APEX maps for all five  $\text{CH}_3\text{OH}$  transitions belonging to the  $J = 5_K - 4_K$  branch (Figure A.2 and Table B.1). The spectra are shown in Figure B.1. For column density calculations, we followed two different treatments: a local thermodynamic equilibrium (LTE) analysis, assuming optically thin emission (Goldsmith & Langer 1999), and a non-LTE study employing the RADEX code (van der Tak et al. 2007). For both methods, a temperature of  $30 \text{ K}$  is assumed (Lindberg & Jørgensen 2012). Although the non-LTE analysis indicates that the  $\text{CH}_3\text{OH}$  lines are not thermalised (see Figure B.3) for densities below  $10^7 \text{ cm}^{-3}$ , and four out of five transitions are optically thick (see Figure B.4), the estimated  $\text{CH}_3\text{OH}$  column densities derived with both methods agree with each other (for typical envelope densities  $n_{\text{H}_2}$  between  $10^5$  and  $10^6 \text{ cm}^{-3}$ ; see Table B.2). More details about the LTE and non-LTE analysis are presented in Appendix B. Table 3 lists the resulting column densities calculated from the LTE analysis and using  $T_{\text{rot}} = 30 \text{ K}$ . The uncertainties were calculated from the spectral rms noise and  $20\%$  calibration uncertainty.

#### 4. Linking methanol ice and gas

In this section, we analyse the gas-ice variations in the Coronet cluster. The  $\text{H}_2\text{O}$  and  $\text{CH}_3\text{OH}$  ice column densi-

Table 3: Total ice and gas column densities ( $N$ ) and fractional abundances ( $X$ ) relative to  $H_2$  towards the Coronet cluster members.

| Object     | $N_{H_2O}^{ice}$ <sup>(a)</sup><br>[ $10^{18} \text{cm}^{-2}$ ] | $N_{CH_3OH}^{ice}$<br>[ $10^{17} \text{cm}^{-2}$ ] | $N_{CH_3OH}^{gas}$ <sup>(b)</sup><br>[ $10^{15} \text{cm}^{-2}$ ] | $N_{H_2}^{SCUBA}$ <sup>(d)</sup><br>[ $10^{23} \text{cm}^{-2}$ ] | $X_{H_2O}^{ice}$<br>[ $10^{-5}$ ] | $X_{CH_3OH}^{ice}$<br>[ $10^{-6}$ ] | $X_{CH_3OH}^{gas}$<br>[ $10^{-8}$ ] |
|------------|---|--|---|--|-----------------------------------|-------------------------------------|-------------------------------------|
| IRS5A      | $3.58 \pm 0.26$   | $2.36 \pm 0.57$                                    | $0.05 \pm 0.02^{(c)}$   | $0.55 \pm 0.06$  | $6.51 \pm 0.80$                   | $4.29 \pm 1.12$                     | $0.09 \pm 0.04$                     |
| HH100 IRS1 | $2.45 \pm 0.24$   | $< 2.38$   | $0.07 \pm 0.03^{(c)}$   | $0.67 \pm 0.07$  | $3.66 \pm 0.51$                   | $< 3.55$                            | $0.10 \pm 0.05$                     |
| SMM1C      | –   | –  | $1.95 \pm 0.23$   | $1.58 \pm 0.16$  | –                                 | –                                   | $1.23 \pm 0.19$                     |
| IRS7A      | $10.89 \pm 1.92$  | $< 4.14$   | $1.28 \pm 0.15$   | $1.48 \pm 0.15$  | $7.36 \pm 1.49$                   | $< 2.98$                            | $0.86 \pm 0.13$                     |
| SMM1A      | –   | –  | $3.54 \pm 0.43$   | $1.90 \pm 0.19$  | –                                 | –                                   | $1.86 \pm 0.29$                     |
| IRS7B      | $11.01 \pm 1.97$  | $7.49 \pm 0.33$                                    | $1.91 \pm 0.23$   | $1.92 \pm 0.19$  | $5.73 \pm 1.18$                   | $3.90 \pm 0.43$                     | $0.99 \pm 0.16$                     |
| SMM2       | –   | –  | $1.64 \pm 0.20$   | $1.09 \pm 0.11$  | –                                 | –                                   | $1.50 \pm 0.24$                     |

**Notes.** <sup>(a)</sup>Boogert et al. (2008). <sup>(b)</sup> $CH_3OH$  column densities calculated using  $T_{rot} = 30$  K. <sup>(c)</sup>Lindberg et al. (2015). <sup>(d)</sup> $H_2$  column densities assuming  $T_{dust} = 30$  K. The errors on the  $H_2$  column densities are estimated from the 10% flux calibration uncertainty at  $850 \mu\text{m}$ . The "–" symbol indicates the sources for which ice column densities and abundances are not available.

ties were determined by Boogert et al. (2008) from *Spitzer* IRS mid-infrared spectra as part of the *Spitzer* Legacy Program "From Molecular Cores to Planet-Forming Disks" (c2d). For the gas-phase counterpart, we made use of  $CH_3OH$  gas column densities calculated in Sect. 3 and reported in Table 3.

#### 4.1. $H_2$ column densities

Prior to searching for gas-ice correlations, the physical structure of the Coronet cluster is investigated by producing an  $H_2$  column density map of the targeted region. This step is required as fractional abundances instead of absolute column densities need to be compared when studying gas-ice variations. This is due to the fact that gas and ice observations, by their very nature, are tracing different spatial scales, and therefore, a comparison between absolute values can lead to misinterpretations (e.g., Noble et al. 2017). At the same time it is important to note that the  $H_2$  column density calculated below provides the total  $H_2$  column density - and hence it traces regions where methanol is in the gas phase as well as in the ices. As a result, the  $CH_3OH$  abundances presented in this work have to be interpreted as "average" abundances.

Figure 4 shows the  $H_2$  column density map of the Coronet cluster obtained by making use of SCUBA submillimeter continuum maps at  $850 \mu\text{m}$  from Nutter et al. (2005). A detailed description of the formalism adopted to obtain the  $H_2$  column density from SCUBA maps is provided in Appendix C of Perotti et al. (2020). Briefly, in an optically thin thermal dust emission regime, the strength of the submillimeter radiation depends on the column density ( $N$ ), the dust temperature ( $T$ ) and the opacity ( $\kappa_\nu$ ) (Kauffmann et al. 2008). The inserted value for the opacity per unit dust+gas mass is  $0.0182 \text{ cm}^2 \text{ g}^{-1}$  ("OH5 dust"; Ossenkopf & Henning 1994). The adopted value for the dust temperature is 30 K, based on previous observational studies of

the Coronet and radiative transfer models by Lindberg & Jørgensen (2012).

The youngest cluster members are all situated in the densest areas of the targeted region (Fig. 4). The apex of the estimated  $H_2$  column density lies to the south-east of R CrA, and in particular at the IRS7B, SMM1A, SMM1C and IRS7A positions ( $N_{H_2} > 1.45 \times 10^{23} \text{ cm}^{-2}$ ). SMM2, IRS1, IRS5N and IRS5A are located in slightly less dense regions ( $0.5 \times 10^{23} \text{ cm}^{-2} < N_{H_2} < 1.25 \times 10^{23} \text{ cm}^{-2}$ ). The measured  $H_2$  column densities and their uncertainties for individual sources are listed in Table 3.

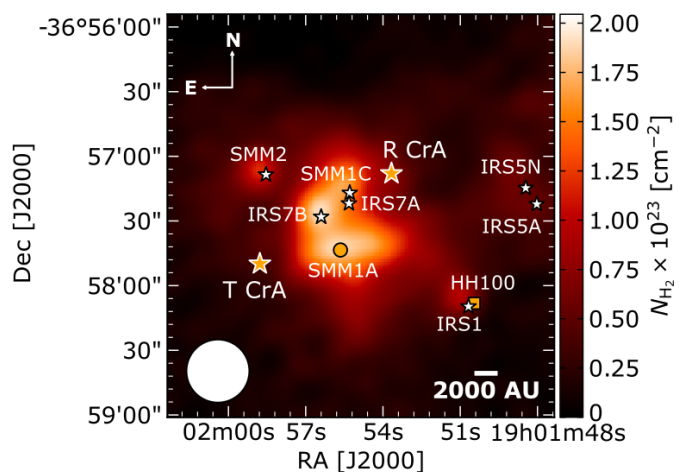


Fig. 4:  $H_2$  column density map of the R CrA region calculated from SCUBA dust emission maps at  $850 \mu\text{m}$  by Nutter et al. (2005). Refer to Fig. 1 for a guide to the symbols of the Coronet cluster objects.

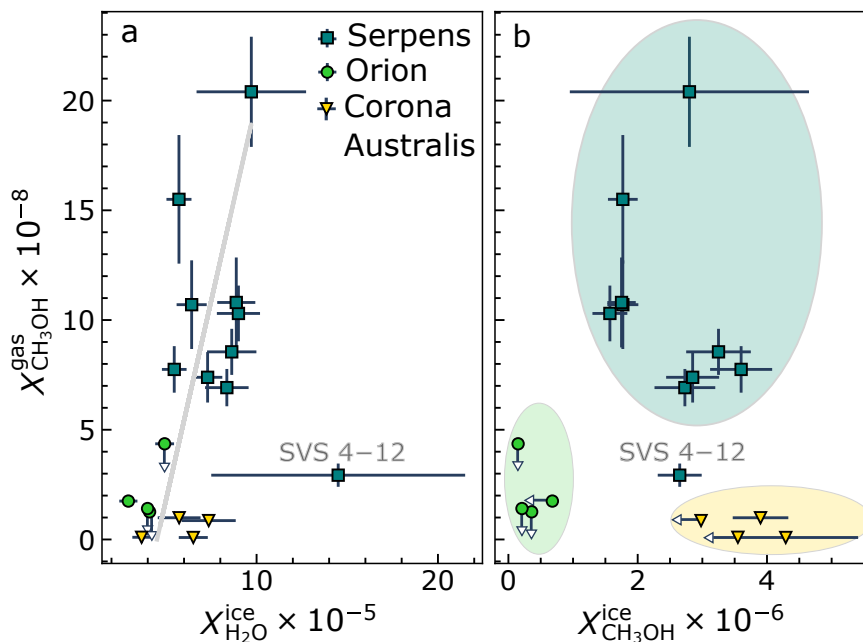


Fig. 5: Relationship between  $\text{CH}_3\text{OH}$  and  $\text{H}_2\text{O}$  fractional abundances ( $X$ ) towards three nearby low-mass star-forming regions. The triangles represent the gas and ice fractional abundances relative to  $\text{H}_2$  for the Coronet cluster members listed in Table 3 for which both gas and ice measurements are available. The squares and circles symbolize the values obtained for Serpens SVS 4 and Orion B35A from Perotti et al. (2020) and Perotti et al. (2021), respectively. The  $\text{CH}_3\text{OH}$  gas abundances are compared to the  $\text{H}_2\text{O}$  (panel a) and  $\text{CH}_3\text{OH}$  (panel b) ice abundances. Upper limits are marked as empty arrows. The grey line in panel a represents the linear fit to the detections. In panel b three different groups are identified, excluding Serpens SVS 4–12; they correspond to the three star-forming regions and they are marked with coloured ovals.

#### 4.2. Gas-ice variations

The analysis of gas-ice variations in the Coronet is addressed by comparing fractional abundances ( $X$ ) of gas and ice species relative to  $\text{H}_2$  (Table 3). In addition, this section also provides an overview of gas-ice variations in the Coronet with respect to two other nearby low-mass star-forming clusters: Serpens SVS 4 and Orion B35A, which have been observed with the same facilities, angular resolution, and receiver settings adopted for observations of the Coronet to assure a meaningful comparison and reduce observational bias (see Perotti et al. 2020, 2021).

Fig. 5 displays  $\text{CH}_3\text{OH}$  gas abundances as function of  $\text{H}_2\text{O}$  (a) and  $\text{CH}_3\text{OH}$  ice (b). A correlation between  $\text{CH}_3\text{OH}$  gas and  $\text{H}_2\text{O}$  ice for the three star-forming regions is seen in panel a with the Coronet cluster showing gas-ice abundances as low as the Orion B35A cloud. The lower methanol gas abundances in the Coronet and in Orion B35A may be due to reduced ice mantle formation and enhanced photodissociation of methanol molecules upon desorption in these two regions with stronger UV field (see Section 5 for more details). The spread among the  $\text{H}_2\text{O}$  abundances for the Coronet cluster and Orion B35A is limited, spanning less than a factor of 2.6 including the uncertainties. The same applies to the  $\text{CH}_3\text{OH}$  gas abundances. In contrast, Serpens SVS 4 exhibits the highest values compared to the other two regions and the largest spread, with  $\text{CH}_3\text{OH}$  gas abundances ranging up to  $\sim 20 \times 10^{-8}$ . One outlier is identified, Serpens SVS 4–12, which is characterized by the lowest  $\text{CH}_3\text{OH}$  gas and highest  $\text{H}_2\text{O}$  ice abundances relative to the other Serpens SVS 4 protostars. This result is not surprising since this is the most extincted ob-

ject of all targeted sources ( $A_V \sim 95$  mag; Pontoppidan et al. 2004) with the lowest S/N (see Perotti et al. 2020 for a detailed discussion on Serpens SVS 4–12).

Fig. 5 b compares  $\text{CH}_3\text{OH}$  gas and ice abundances. In contrast to panel a, no clear trend is seen. However, when Serpens SVS 4–12 is excluded from the analysis it is possible to identify three different groups corresponding to the three regions: i) Orion B35A with the lowest measurements of both  $\text{CH}_3\text{OH}$  in the gas and in the solid state; ii) Serpens SVS 4 with intermediate to high values of  $\text{CH}_3\text{OH}$  ice and the highest gas abundances, and finally iii) the Coronet cluster, with some of the highest  $\text{CH}_3\text{OH}$  ice but surprisingly low  $\text{CH}_3\text{OH}$  gas abundances. The observed behaviour for the Coronet cluster is likely due to  $\text{CH}_3\text{OH}$  destruction in the gas phase as a consequence of strong external irradiation (Lindberg & Jørgensen 2012).

Figure 6 shows  $\text{H}_2\text{O}$  (a) and  $\text{CH}_3\text{OH}$  (b) ice column densities ( $N$ ) as function of cloud visual extinction ( $A_V$ ) for lines of sights in the three nearby star-forming clusters. The cloud extinction estimates were taken from Pontoppidan et al. (2004) for Serpens SVS 4, from Perotti et al. (2021) for Orion B35A, and from Alves et al. (2014) for the Coronet cluster, then converted to visual extinction using the conversion factors (3.6 for  $A_J$ , 5.55 for  $A_H$  and 8.33 for  $A_K$ ) from Weingartner & Draine (2001) for  $RV = 5.5$  for the dense ISM.

The distribution of data points in panels a and b shows a positive trend for Serpens SVS 4 and Orion B35A, indicating that to higher visual extinctions correspond higher columns of  $\text{H}_2\text{O}$  (a) and  $\text{CH}_3\text{OH}$  (b). This observation is particularly valid for  $\text{H}_2\text{O}$  but it also applies to  $\text{CH}_3\text{OH}$

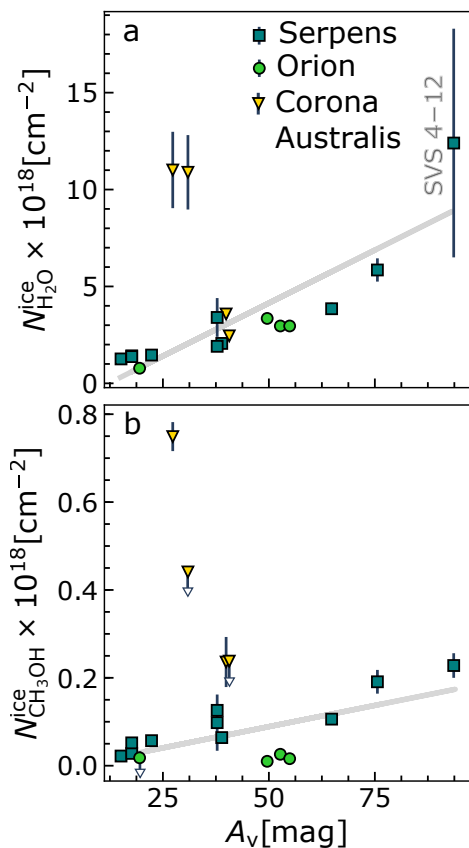


Fig. 6: Relationship between H<sub>2</sub>O (a), CH<sub>3</sub>OH (b) ice column densities ( $N$ ) and visual extinction ( $A_V$ ) for lines of sights in nearby star-forming clusters: the Coronet in Corona Australis (triangles), Serpens SVS 4 (squares), and Orion B35A (circles). Upper limits are marked as arrows. The gray lines represent linear fits to the detections. We note that the visual extinction values obtained for Corona Australis have to be taken with care as their determination is hampered by the lack of background stars towards the densest region of the Coronet cluster (see Section 4.2). The data for Serpens SVS 4 and Orion B35A were taken from Perotti et al. (2020) and Perotti et al. (2021), respectively.

when an evaluation is done per star-forming region. The opposite behaviour is found for the Coronet cluster members, for both ice species. This negative trend could simply reflect inaccurate extinction values due to the lack of background stars in the densest area of the Corona Australis complex, where the Coronet cluster members are located (see Section 2 of Alves et al. (2014) for more details).

## 5. Discussion

In this study, the CH<sub>3</sub>OH chemical behavior has been investigated with millimetric and infrared facilities. This provides direct observational constraints on the CH<sub>3</sub>OH gas-to-ice ratio in protostellar envelopes and on its dependency on the physical conditions of star-forming regions. Laboratory experiments predict that CH<sub>3</sub>OH ice in cold dark clouds is non-thermally desorbed with an efficiency spanning over approximately three orders of magnitude ( $10^{-6} - 10^{-3}$  molecules/photon; Öberg et al. 2009b; Bertin et al. 2016; Cruz-Díaz et al. 2016; Martín-

Doménech et al. 2016). This range is expected to increase up to  $\sim 10^{-2}$  molecules/photon (Basalgète et al. 2021a,b), as X-rays emitted from the central YSO strongly impact the abundances of CH<sub>3</sub>OH in protostellar envelopes (Notsu et al. 2021). Generally, the majority of non-thermally desorbed CH<sub>3</sub>OH molecules fragment during the desorption and a fraction of those recombine (e.g., Bertin et al. 2016). The CH<sub>3</sub>OH non-thermal desorption efficiency and by inference the gas-to-ice ratio is highly dependent on the ice structure and composition (pure CH<sub>3</sub>OH versus CH<sub>3</sub>OH mixed with CO molecules), as well as on the temperature, photon energy and flux (e.g., Öberg 2016; Carrascosa et al. 2023). To support laboratory experiments and computations, in this paper we provide observational measurements of the CH<sub>3</sub>OH gas-to-ice ratio in the outer regions of protostellar envelopes.

Our targeted regions (Serpens SVS 4, Orion B35A and Corona Australis Coronet) share a number of similarities: e.g., they are low-mass star forming regions, they are clustered and finally, they are affected by the presence of outflows and/or Herbig-Haro objects. However, they show distinct physical conditions for instance, the Serpens SVS 4 cluster is influenced by the presence of the Class 0 binary SMM4 (Pontoppidan et al. 2004), whereas B35A is affected by the nearby high-mass star  $\lambda$  Orionis (Reipurth & Friberg 2021) and the Coronet is strongly irradiated by the Herbig Ae/Be star R CrA (Lindberg & Jørgensen 2012). B35A is exposed to an interstellar radiation field  $\chi_{\text{ISRF}}$  of 34 (Wolfire et al. 1989)<sup>3</sup> enhanced by the neighbouring  $\lambda$  Orionis (Dolan & Mathieu 2002), whereas the radiation field in the Coronet cluster has been estimated to approximately  $\chi_{\text{ISRF}} \sim 750$  to account for the high fluxes at millimeter wavelengths (Lindberg & Jørgensen 2012).

In addition, the molecular clouds in which our targeted regions are located do not share a common formation history. The ongoing low-mass star formation in Serpens Main might have been triggered by cloud-cloud collisions (Duarte-Cabral et al. 2010) or compression from a shock wave from a supernova. However, there is no clear evidence that a nearby supernova ever occurred (Herczeg et al. 2019). In contrast to Serpens, the formation of the ring constituting the  $\lambda$  Orionis region is attributed to a supernova explosion that occurred roughly 1–6 Myr ago (Dolan & Mathieu 1999, 2002; Kounkel 2020). The low-mass star formation in B35A was likely generated by the presence of neighboring massive stars and their stellar winds (Barrado et al. 2018). Finally, star-formation in Corona Australis has been supposedly promoted by a high-velocity cloud impact onto the Galactic plane (Neuhäuser & Forbrich 2008) or by the expansion of the UpperCenLupus (UCL) superbubble (Mamajek et al. 2002). The fact that the three regions likely did not form in the same way implies different initial physical conditions for the production of CH<sub>3</sub>OH.

Figure 7 illustrates the distribution of the CH<sub>3</sub>OH gas-to-ice ratios ( $N_{\text{gas}}/N_{\text{ice}}$ ) towards low-mass protostars located in the different molecular clouds described above. The average CH<sub>3</sub>OH gas-to-ice ratio ( $1.2 \times 10^{-4}$ ) determined from millimetric (single-dish) and infrared measurements by Öberg et al. (2009a) for four Class 0/I sources in Perseus, Taurus and Serpens is over-plotted. A de-

<sup>3</sup> Note that Wolfire et al. (1989) report a  $\log(G_0)$  of 1.3 which is here converted to  $\chi_{\text{ISRF}}$  by applying the formalism described by Draine & Bertoldi (1996).



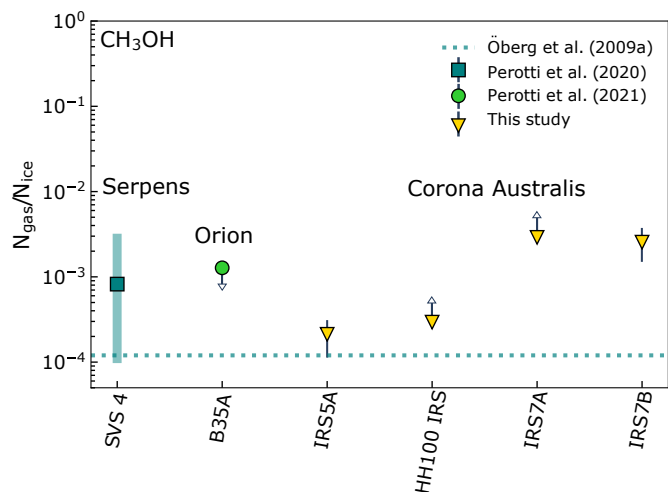


Fig. 7:  $\text{CH}_3\text{OH}$  gas-to-ice ratios ( $N_{\text{gas}}/N_{\text{ice}}$ ) towards low-mass protostars in the Coronet cluster in Corona Australis (triangles). The square and the circle symbolize the average ratios for ten sources in Serpens SVS 4 and four sources in Orion B35A, respectively. The green shaded area corresponds to the interval of gas-to-ice ratios observed for the ten sources in the Serpens SVS 4 cluster. The dotted line indicates the average value for four sources from Öberg et al. (2009a). Upper and lower limits are marked as arrows.

tailed comparison between the gas-to-ice ratio determined by Öberg et al. (2009a) and the ratios calculated for the sources in the Serpens SVS 4 and the Orion B35A cloud is provided in Perotti et al. (2021). In this section we focus on the ratios obtained for Corona Australis and their comparison with the values determined for the two other star-forming regions.

The distribution of  $\text{CH}_3\text{OH}$  gas-to-ice ratios towards the Coronet cluster covers approximately one order of magnitude. The uncertainty on the determination of the  $\text{CH}_3\text{OH}$  ice column densities for HH100 IRS1 and IRS7A (Boogert et al. 2008) results in lower limits for their gas-to-ice ratios, consequently we can not provide solid comparisons for these two sources. In contrast, the values obtained for IRS5A and IRS7B fall in the range of gas-to-ice ratios previously obtained for the protostars located in the Serpens SVS 4 cluster.

The  $\text{CH}_3\text{OH}$  gas-to-ice ratios constrained from gas and ice observations of a sample of protostellar envelopes (Figure 7) do not point to one value but, instead, to a distribution ( $1.2 \times 10^{-4}$  to  $3.1 \times 10^{-3}$ ) which validates previous observational studies (e.g., Öberg et al. 2009a; Perotti et al. 2020). This distribution agrees with a more complex scenario for the  $\text{CH}_3\text{OH}$  desorption elucidated in the laboratory in which a large fraction of  $\text{CH}_3\text{OH}$  molecules do not desorb intact, but instead fragment and eventually recombine during and after the desorption (e.g., Bertin et al. 2016) leading to  $\text{CH}_3\text{OH}$  gas-to-ice ratios lower than  $10^{-3}$ .

A second interesting observation is that the  $\text{CH}_3\text{OH}$  gas-to-ice ratios fall in a fairly narrow range; this suggests that the  $\text{CH}_3\text{OH}$  chemistry at play in the cold outer regions of protostellar envelopes belonging to different low-mass star-forming regions is relatively independent of variations in the physical conditions. We note that a similar

conclusion could not be tested for the innermost envelope regions where thermal desorption dominates and young disks are present; our observations are simply not sensitive to these regions. Our analysis implicitly indicates that the  $\text{CH}_3\text{OH}$  chemistry in the outer envelope regions is set to a large degree already during the prestellar stage. A related result came to light when comparing abundances of complex organic molecules observed in distinct star-forming environments (e.g., Galactic disc versus Galactic center, high-mass versus low-mass star-forming region; Jørgensen et al. 2020; Coletta et al. 2020; Yang et al. 2021; Nazari et al. 2022a). A larger sample is however necessary to prove this statement, and additional observations, laboratory experiments and modelling efforts are required to elucidate further the impact of the physical evolution of protostars on their chemical signatures and vice versa.

## 6. Conclusions

We present 1.3 mm SMA and APEX observations towards the Coronet cluster in Corona Australis, a unique astrochemical laboratory to study the effect of external irradiation on the chemical and physical evolution of young protostars. In addition, we determined  $\text{CH}_3\text{OH}$  gas-phase abundances and compared those with  $\text{CH}_3\text{OH}$  ice abundances from Boogert et al. (2008) to directly constrain the  $\text{CH}_3\text{OH}$  gas-to-ice ratio in cold protostellar envelopes. Our key findings are:

- We find a positive trend between  $\text{H}_2\text{O}$  ice and  $\text{CH}_3\text{OH}$  gas abundances in Serpens SVS 4, Coronet, and Orion B35A with the latter two regions showing the lowest gas abundances. This result is attributed to reduced ice mantle formation and substantial destruction of methanol gas molecules in these two regions characterized by stronger external UV field.
- The distribution of  $\text{CH}_3\text{OH}$  gas-to-ice ratios in the Coronet constrained from millimetric and infrared observations spans over one order of magnitude and reinforces previous observational constraints on the  $\text{CH}_3\text{OH}$  gas-to-ice ratio.
- Similarities are found between  $\text{CH}_3\text{OH}$  gas-to-ice ratios determined in different low-mass star forming regions (Serpens SVS 4, Orion B35A and Coronet), characterized by distinct physical conditions and formation histories. This result suggests that the  $\text{CH}_3\text{OH}$  chemistry - in the outer regions of low-mass envelopes - is relatively independent of variations in the physical conditions and thus it is set to a large degree during the prestellar stage.

Multiple avenues for future studies can be pursued. Comparisons of gas and ice abundances of key species are currently limited by the low number of infrared surveys. Current infrared facilities such as the *James Webb* Space Telescope are now routinely probing interstellar ices towards background stars (McClure et al. 2023), pre-stellar cores, proto-stellar envelopes (Yang et al. 2022) and near edge-on discs (Sturm et al. 2023), thus significantly increasing the number of studied regions. Therefore, it will be feasible to search for gas-ice trends found in other regions, improve our constraints on the  $\text{CH}_3\text{OH}$  gas-to-ice ratios, and ultimately determine ratios for a larger set of major

interstellar molecules. This approach will provide important feedback on the interactions between ice and gas material during its journey from the molecular cloud to the disc and on the impact of the physical conditions on the physico-chemical evolution of protostars. In this context, the Corona Australis complex still has much to teach us, hosting one of the youngest population of protostars observed so far.

*Acknowledgements.* We thank Chunhua Qi for translating the SMA data into a format readable in CASA, Henrik Olofsson, and Dirk Petry for guidance in importing the APEX data to CASA and the anonymous reviewer for the careful reading of the manuscript and the useful comments. This work is based on observations with the Submillimeter Array, Mauna Kea, Hawaii, program codes: 2019B-S014 and 2020B-S058 (PI: Perotti) and with the Atacama Pathfinder Experiment, Llano Chajnantor, Chile, program code: 0105.F-9300 (PI: Perotti). The Submillimeter Array is a joint project between the Smithsonian Astrophysical Observatory and the Academia Sinica Institute of Astronomy and Astrophysics and is funded by the Smithsonian Institution and the Academia Sinica. The Atacama Pathfinder EXperiment (APEX) telescope is a collaboration between the Max Planck Institute for Radio Astronomy, the European Southern Observatory, and the Onsala Space Observatory. Swedish observations on APEX are supported through Swedish Research Council grant No 2017-00648. This publication also makes use of data products from the Wide-field Infrared Survey Explorer, which is a joint project of the University of California, Los Angeles, and the Jet Propulsion Laboratory/California Institute of Technology, funded by the National Aeronautics and Space Administration. GP gratefully acknowledges support from the Max Planck Society. The research of MS is supported by NASA under award number 80GSFC21M0002. JJK acknowledges support from the Independent Research Fund Denmark (grant number 0135-00123B). EAdIV acknowledges financial support provided by FONDECYT grant 3200797. HJF gratefully acknowledges the support of STFC for Astrochemistry at the OU under grant Nos ST/P000584/1 and ST/T005424/1 enabling her participation in this work. SBC was supported by the NASA Planetary Science Division Internal Scientist Funding Program through the Fundamental Laboratory Research work package (FLaRe). The authors wish to recognize and acknowledge the very significant cultural role and reverence that the summit of Mauna Kea has always had within the indigenous Hawaiian community. We are most fortunate to have the opportunity to conduct observations from this mountain.

## References

- Alves, F. O., Cleeves, L. I., Girart, J. M., et al. 2020, *ApJ*, 904, L6  
 Alves, J., Lombardi, M., & Lada, C. J. 2014, *A&A*, 565, A18  
 Andrews, S. M., Huang, J., Pérez, L. M., et al. 2018, *ApJ*, 869, L41  
 Artur de la Villarmois, E., Kristensen, L. E., Jørgensen, J. K., et al. 2018, *A&A*, 614, A26  
 Balucani, N., Ceccarelli, C., & Taquet, V. 2015, *MNRAS*, 449, L16  
 Barrado, D., de Gregorio Monsalvo, I., Huélamo, N., et al. 2018, *A&A*, 612, A79  
 Basalgète, R., Dupuy, R., Féraud, G., et al. 2021a, *A&A*, 647, A35  
 Basalgète, R., Dupuy, R., Féraud, G., et al. 2021b, *A&A*, 647, A36  
 Bean, B., Bhatnagar, S., Castro, S., et al. 2022, *Publications of the Astronomical Society of the Pacific*, 134, 114501  
 Bertin, M., Romanzin, C., Doronin, M., et al. 2016, *ApJ*, 817, L12  
 Bibo, E. A., The, P. S., & Dawanas, D. N. 1992, *A&A*, 260, 293  
 Boogert, A. C. A., Gerakines, P. A., & Whittet, D. C. B. 2015, *ARA&A*, 53, 541  
 Boogert, A. C. A., Pontoppidan, K. M., Knez, C., et al. 2008, *ApJ*, 678, 985  
 Bottinelli, S., Boogert, A. C. A., Bouwman, J., et al. 2010, *ApJ*, 718, 1100  
 Carrascosa, H., Satorre, M. Á., Escribano, B., Martín-Doménech, R., & Muñoz Caro, G. M. 2023, arXiv e-prints, arXiv:2308.05980  
 Cazzoletti, P., Manara, C. F., Baobab Liu, H., et al. 2019, *A&A*, 626, A11  
 Chen, X. & Arce, H. G. 2010, *ApJ*, 720, L169  
 Chuang, K. J., Fedoseev, G., Ioppolo, S., van Dishoeck, E. F., & Linnartz, H. 2016, *MNRAS*, 455, 1702  
 Coletta, A., Fontani, F., Rivilla, V. M., et al. 2020, *A&A*, 641, A54  
 Cruz-Díaz, G. A., Martín-Doménech, R., Muñoz Caro, G. M., & Chen, Y.-J. 2016, *A&A*, 592, A68  
 Dib, S. & Henning, T. 2019, *A&A*, 629, A135  
 Dolan, C. J. & Mathieu, R. D. 1999, *AJ*, 118, 2409  
 Dolan, C. J. & Mathieu, R. D. 2002, *AJ*, 123, 387  
 Draine, B. T. & Bertoldi, F. 1996, *ApJ*, 468, 269  
 Duarte-Cabral, A., Fuller, G. A., Peretto, N., et al. 2010, *A&A*, 519, A27  
 Endres, C. P., Schlemmer, S., Schilke, P., Stutzki, J., & Müller, H. S. P. 2016, *Journal of Molecular Spectroscopy*, 327, 95  
 Esplin, T. L. & Luhman, K. L. 2022, *AJ*, 163, 64  
 Fedoseev, G., Chuang, K. J., Ioppolo, S., et al. 2017, *ApJ*, 842, 52  
 Forbrich, J. & Preibisch, T. 2007, *A&A*, 475, 959  
 Forbrich, J., Preibisch, T., Menten, K. M., et al. 2007, *A&A*, 464, 1003  
 Fuchs, G. W., Cuppen, H. M., Ioppolo, S., et al. 2009, *A&A*, 505, 629  
 Galli, P. A. B., Bouy, H., Olivares, J., et al. 2020, *A&A*, 634, A98  
 Garrod, R. T. & Herbst, E. 2006, *A&A*, 457, 927  
 Geppert, W. D., Hamberg, M., Thomas, R. D., et al. 2006, *Faraday Discussions*, 133, 177  
 Goldsmith, P. F. & Langer, W. D. 1999, *ApJ*, 517, 209  
 Gray, R. O., Corbally, C. J., Garrison, R. F., et al. 2006, *AJ*, 132, 161  
 Groppi, C. E., Hunter, T. R., Blundell, R., & Sandell, G. 2007, *ApJ*, 670, 489  
 Güsten, R., Nyman, L. Å., Schilke, P., et al. 2006, *A&A*, 454, L13  
 Harsono, D., Bjerkeli, P., van der Wiel, M. H. D., et al. 2018, *Nature Astronomy*, 2, 646  
 Haworth, T. J., Kim, J. S., Winter, A. J., et al. 2021, *MNRAS*, 501, 3502  
 Herbig, G. H. 1960, *ApJS*, 4, 337  
 Herczeg, G. J., Kuhn, M. A., Zhou, X., et al. 2019, *ApJ*, 878, 111  
 Ho, P. T. P., Moran, J. M., & Lo, K. Y. 2004, *ApJ*, 616, L1  
 Jørgensen, J. K., Belloche, A., & Garrod, R. T. 2020, *ARA&A*, 58, 727  
 Kauffmann, J., Bertoldi, F., Bourke, T. L., Evans, N. J., I., & Lee, C. W. 2008, *A&A*, 487, 993  
 Keane, J. V., Tielens, A. G. G. M., Boogert, A. C. A., Schutte, W. A., & Whittet, D. C. B. 2001, *A&A*, 376, 254  
 Keppler, M., Benisty, M., Müller, A., et al. 2018, *A&A*, 617, A44  
 Kounkel, M. 2020, *ApJ*, 902, 122  
 Kristensen, L. E., van Dishoeck, E. F., van Kempen, T. A., et al. 2010, *A&A*, 516, A57  
 Kuffmeier, M., Zhao, B., & Caselli, P. 2020, *A&A*, 639, A86  
 Lindberg, J. E. & Jørgensen, J. K. 2012, *A&A*, 548, A24  
 Lindberg, J. E., Jørgensen, J. K., Brinch, C., et al. 2014, *A&A*, 566, A74  
 Lindberg, J. E., Jørgensen, J. K., Watanabe, Y., et al. 2015, *A&A*, 584, A28  
 Mamajek, E. E., Meyer, M. R., & Liebert, J. 2002, *AJ*, 124, 1670  
 Martín-Doménech, R., Muñoz Caro, G. M., & Cruz-Díaz, G. A. 2016, *A&A*, 589, A107  
 McClure, M. K., Rocha, W. R. M., Pontoppidan, K. M., et al. 2023, *Nature Astronomy*, 7, 431  
 McGuire, B. A. 2022, *ApJS*, 259, 30  
 McMullin, J. P., Waters, B., Schiebel, D., Young, W., & Golap, K. 2007, in *Astronomical Society of the Pacific Conference Series*, Vol. 376, *Astronomical Data Analysis Software and Systems XVI*, ed. R. A. Shaw, F. Hill, & D. J. Bell, 127  
 Mesa, D., Bonnefoy, M., Gratton, R., et al. 2019, *A&A*, 624, A4  
 Miettinen, O., Kontinen, S., Harju, J., & Higdon, J. L. 2008, *A&A*, 486, 799  
 Müller, H. S. P., Schlöder, F., Stutzki, J., & Winnewisser, G. 2005, *Journal of Molecular Structure*, 742, 215  
 Müller, H. S. P., Thorwirth, S., Roth, D. A., & Winnewisser, G. 2001, *A&A*, 370, L49  
 Nazari, P., Meijerhof, J. D., van Gelder, M. L., et al. 2022a, *A&A*, 668, A109  
 Nazari, P., Tabone, B., Rosotti, G. P., et al. 2022b, *A&A*, 663, A58  
 Neuhäuser, R. & Forbrich, J. 2008, *The Corona Australis Star Forming Region*, Vol. 5 (Reipurth, B.), 735  
 Noble, J. A., Fraser, H. J., Pontoppidan, K. M., & Craighan, A. M. 2017, *MNRAS*, 467, 4753  
 Notsu, S., van Dishoeck, E. F., Walsh, C., Bosman, A. D., & Nomura, H. 2021, *A&A*, 650, A180  
 Nutter, D. J., Ward-Thompson, D., & André, P. 2005, *MNRAS*, 357, 975  
 Öberg, K. I. 2016, *Chemical Reviews*, 116, 9631, pMID: 27099922  
 Öberg, K. I., Bottinelli, S., & van Dishoeck, E. F. 2009a, *A&A*, 494, L13  
 Öberg, K. I., Garrod, R. T., van Dishoeck, E. F., & Linnartz, H. 2009b, *A&A*, 504, 891  
 Ossenkopf, V. & Henning, T. 1994, *A&A*, 291, 943  
 Pentead, E. M., Walsh, C., & Cuppen, H. M. 2017, *ApJ*, 844, 71  
 Perotti, G., Jørgensen, J. K., Fraser, H. J., et al. 2021, *A&A*, 650, A168  
 Perotti, G., Rocha, W. R. M., Jørgensen, J. K., et al. 2020, *A&A*, 643, A48  
 Peterson, D. E., Caratti o Garatti, A., Bourke, T. L., et al. 2011, *ApJS*, 194, 43  
 Pickett, H. M., Poynter, R. L., Cohen, E. A., et al. 1998, *J. Quant. Spectr. Rad. Transf.*, 60, 883  
 Pineda, J. E., Arzoumanian, D., Andre, P., et al. 2023, in *Astronomical Society of the Pacific Conference Series*, Vol. 534, *Astronomical Society of the Pacific Conference Series*, ed. S. Inutsuka, Y. Aikawa, T. Muto, K. Tomida, & M. Tamura, 233  
 Pontoppidan, K. M., Boogert, A. C. A., Fraser, H. J., et al. 2008, *ApJ*, 678, 1005  
 Pontoppidan, K. M., Fraser, H. J., Dartois, E., et al. 2003, *A&A*, 408, 981

- Pontoppidan, K. M., van Dishoeck, E. F., & Dartois, E. 2004, *A&A*, 426, 925
- Qasim, D., Chuang, K.-J., Fedoseev, G., et al. 2018, *A&A*, 612, A83
- Rabli, D. & Flower, D. R. 2010, *MNRAS*, 406, 95
- Reipurth, B. & Friberg, P. 2021, *MNRAS*, 501, 5938
- Roberts, H. & Millar, T. J. 2000, *A&A*, 364, 780
- Santos, J. C., Chuang, K.-J., Lamberts, T., et al. 2022, *ApJ*, 931, L33
- Schöier, F. L., Jørgensen, J. K., Pontoppidan, K. M., & Lundgren, A. A. 2006, *A&A*, 454, L67
- Schöier, F. L., van der Tak, F. F. S., van Dishoeck, E. F., & Black, J. H. 2005, *A&A*, 432, 369
- Segura-Cox, D. M., Schmiedeke, A., Pineda, J. E., et al. 2020, *Nature*, 586, 228
- Shannon, R. J., Cossou, C., Loison, J.-C., et al. 2014, *RSC Advances*, 4, 26342
- Sicilia-Aguilar, A., Henning, T., Kainulainen, J., & Roccatagliata, V. 2011, *The Astrophysical Journal*, 736, 137
- Siebenmorgen, R. & Gredel, R. 1997, *ApJ*, 485, 203
- Simons, M. A. J., Lamberts, T., & Cuppen, H. M. 2020, *A&A*, 634, A52
- Sturm, J. A., McClure, M. K., Beck, T. L., et al. 2023, *A&A*, submitted
- Taylor, K. N. R. & Storey, J. W. V. 1984, *MNRAS*, 209, 5P
- Tychoniec, Ł., Manara, C. F., Rosotti, G. P., et al. 2020, *A&A*, 640, A19
- Tychoniec, Ł., van Dishoeck, E. F., van't Hoff, M. L. R., et al. 2021, *A&A*, 655, A65
- van der Tak, F. F. S., Black, J. H., Schöier, F. L., Jansen, D. J., & van Dishoeck, E. F. 2007, *A&A*, 468, 627
- van Dishoeck, E. F. & Bergin, E. A. 2020, *arXiv e-prints*, arXiv:2012.01472
- van Gelder, M. L., Nazari, P., Tabone, B., et al. 2022, *A&A*, 662, A67
- van Terwisga, S. E., van Dishoeck, E. F., Mann, R. K., et al. 2020, *A&A*, 640, A27
- Wang, H., Mundt, R., Henning, T., & Apai, D. 2004, *ApJ*, 617, 1191
- Watanabe, N. & Kouchi, A. 2002, *ApJ*, 571, L173
- Watanabe, Y., Sakai, N., Lindberg, J. E., et al. 2012, *ApJ*, 745, 126
- Weingartner, J. C. & Draine, B. T. 2001, *ApJ*, 548, 296
- Winter, A. J., Kruijssen, J. M. D., Chevance, M., Keller, B. W., & Longmore, S. N. 2020, *MNRAS*, 491, 903
- Wolfire, M. G., Hollenbach, D., & Tielens, A. G. G. M. 1989, *ApJ*, 344, 770
- Wright, E. L., Eisenhardt, P. R. M., Mainzer, A. K., et al. 2010, *AJ*, 140, 1868
- Xu, L.-H., Fisher, J., Lees, R., et al. 2008, *J. Mol. Spectrosc.*, 251, 305
- Yang, Y.-L., Green, J. D., Pontoppidan, K. M., et al. 2022, *ApJ*, 941, L13
- Yang, Y.-L., Sakai, N., Zhang, Y., et al. 2021, *ApJ*, 910, 20

## Appendix A: Overview of molecular line detections

This section reports the primary beam corrected integrated intensity (moment zero) maps of the species detected in the SMA data set (Figures A.1–A.3). For our molecule of interest, CH<sub>3</sub>OH, we also include in Fig. A.2 the combined SMA+APEX integrated intensity maps. Please refer to Appendix B.1 of Perotti et al. (2020) for a detailed description of the feathering procedure used to combine interferometric and single-dish data.

The eighteen molecular transitions of seven species identified in the SMA data sets are listed in Table A.1. The detected species are: carbon monoxide (<sup>12</sup>CO, <sup>13</sup>CO and C<sup>18</sup>O), formaldehyde (H<sub>2</sub>CO), methanol (CH<sub>3</sub>OH), sulfur oxide (SO), sulfur dioxide (SO<sub>2</sub>), cyclopropenylidene (c-C<sub>3</sub>H<sub>2</sub>), and cyanoacetylene (HC<sub>3</sub>N). The line emission is predominantly extended and it does not necessarily coincide with the position of the compact continuum sources in the Coronet cluster (Figures A.1–A.3). In contrast, it is mostly localized to the east of the Herbig Ae/Be star R CrA and to the south of the young stellar objects IRS7A and IRS7B, at the pre-stellar core SMM1A position. This statement applies especially to H<sub>2</sub>CO and CH<sub>3</sub>OH, and is consistent with previous 1.3 mm SMA observations of the region by Lindberg & Jørgensen (2012) covering the 216.849–218.831 GHz and 226.849–228.831 GHz frequencies ranges. Interestingly, no molecular line emission was detected towards SMM1A in the SMA data set presented by Chen & Arce (2010), although the same number of antennas and configuration were used and the SMA correlator covered spectral ranges similar to the ones presented in this work. However, the SMA observations by Chen & Arce (2010) were designed to study the dust continuum and they were characterized by a shorter bandwidth and likely lower line sensitivity. Unfortunately, a comparison of the line sensitivity of the two data sets could not be made as this information is not reported in Chen & Arce (2010) and a reduced, continuum-subtracted spectrum is not provided either.

The detected species in the SMA data can be roughly divided into three groups described based on their emission pattern (Table A.1): (I) CO species, (II) S-species, and (III) carbon-chain species. Overall, the emission reported in the SMA data set is dominated by molecular tracers such as H<sub>2</sub>CO, CH<sub>3</sub>OH, SO, SO<sub>2</sub>. The emission of H<sub>2</sub>CO and CH<sub>3</sub>OH is consistent with temperature variations in the field of view of the observations, and particularly with the external irradiation from the variable stars in the region (R CrA and T CrA). In contrast, the shock tracers (SO, SO<sub>2</sub>) probe the numerous outflows and Herbig-Haro objects in the region, which are indicators of a young stellar population in the earliest evolutionary stages.

### Appendix A.1: CO-species

Figure A.1 displays the SMA primary beam corrected integrated intensity maps for <sup>12</sup>CO, <sup>13</sup>CO, C<sup>18</sup>O and H<sub>2</sub>CO. The distribution of the CO-species emission is extended, especially for <sup>12</sup>CO and its isotopologues. The three transitions of H<sub>2</sub>CO show the same emission pattern (Figure A.1, panels d–f). The emission is localized in two ridges: the northern ridge between R CrA and SMM1C, and the southern ridge to the south of IRS7B, in the vicinity

of SMM1A. No bright line emission is observed towards the young stellar objects SMM1C, IRS7A and IRS7B. The emission offset from the YSO positions and the elongated shape of the ridges have been previously identified in this region and interpreted as indicators of external heating (Lindberg & Jørgensen 2012). The emission localized in the southern ridge traces the three condensations within the pre-stellar core SMM1A (SMM1A-a, SMM1A-b, and SMM1A-c), analysed in dust continuum observations by Chen & Arce (2010).

The strength of the H<sub>2</sub>CO emission, for the three detected H<sub>2</sub>CO lines is comparable in both ridges. A similar morphology pattern is observed for CH<sub>3</sub>OH where the emission peak is located within the SMM1A core. However, neither the CH<sub>3</sub>OH  $J=4_2 - 3_1$  line nor the CH<sub>3</sub>OH transitions belonging to the  $J = 5_K - 4_K$  branch show a northern ridge (Figures 3 and A.2).

### Appendix A.2: S-species

The SO and SO<sub>2</sub> line emissions appear relatively bright and compact (Figure A.3, panels m–o). The distribution of the emission is identical for the two SO transitions, and it peaks towards IRS7A and SMM1C. The strength of the emission among the SO transitions is very similar (7–8 Jy beam<sup>-1</sup> km s<sup>-1</sup>; Figure A.3, panels m–n). The SO<sub>2</sub> emission is concentrated towards IRS7A and is approximately a factor of 2.5 fainter compared to SO (Figure A.3, panels o). In contrast to the majority of the CO-species, the S-species emission have their strongest emission associated with the YSO positions. SO and SO<sub>2</sub> are molecular tracers of energetic inputs in the form of outflows and jets. The luminous SO and SO<sub>2</sub> emissions appear to indicate that higher velocity ( $\sim 5 - 10$  km s<sup>-1</sup>) flows of matter are present in the field-of-view of the observations, associated with IRS7A and SMM1C. This result is in agreement with studies of the Herbig-Haro objects in the Coronet attributed to SMM1C (Wang et al. 2004; Peterson et al. 2011).

### Appendix A.3: Carbon-chain species

The third group of lines corresponds to carbon-chain species like c-C<sub>3</sub>H<sub>2</sub> and HC<sub>3</sub>N which show a fairly weak emission (1.6–3.0 Jy beam<sup>-1</sup> km s<sup>-1</sup>) compared to the previous two groups (CO- and S-species). Their emission is diffuse and characterized by a fairly low S/N (Figure A.3, panels p–r). Similarly to <sup>13</sup>CO and C<sup>18</sup>O, the carbon-chain species have their brightest emission associated with IRS7B.

Table A.1: Identified molecular transitions in the SMA data set.

| Species                                 | Transition                                     | Frequency <sup>(a)</sup><br>[GHz] | $A_{ul}^{(a)}$<br>[s <sup>-1</sup> ] | $E_u^{(a)}$<br>[K] |
|---|--|-----------------------------------|--------------------------------------|--------------------|
| CO-species                              |  |                                   |                                      |                    |
| <sup>12</sup> CO                        | 2 – 1  | 230.538                           | $6.92 \times 10^{-7}$                | 17                 |
| C <sup>18</sup> O                       | 2 – 1  | 219.560                           | $6.01 \times 10^{-7}$                | 16                 |
| <sup>13</sup> CO                        | 2 – 1  | 220.398                           | $6.04 \times 10^{-7}$                | 16                 |
| H <sub>2</sub> CO                       | 3 <sub>0,3</sub> – 2 <sub>0,2</sub>            | 218.222                           | $2.82 \times 10^{-4}$                | 21                 |
| H <sub>2</sub> CO                       | 3 <sub>2,2</sub> – 2 <sub>2,1</sub>            | 218.476                           | $1.58 \times 10^{-4}$                | 68                 |
| H <sub>2</sub> CO                       | 3 <sub>2,1</sub> – 2 <sub>2,0</sub>            | 218.760                           | $1.58 \times 10^{-4}$                | 68                 |
| CH <sub>3</sub> OH                      | 4 <sub>2</sub> – 3 <sub>1</sub> , E            | 218.440                           | $4.68 \times 10^{-5}$                | 46                 |
| CH <sub>3</sub> OH <sup>b</sup>         | 5 <sub>+0</sub> – 4 <sub>+0</sub> E            | 241.700                           | $6.04 \times 10^{-5}$                | 47.9               |
| CH <sub>3</sub> OH <sup>b</sup>         | 5 <sub>-1</sub> – 4 <sub>-1</sub> E            | 241.767                           | $5.81 \times 10^{-5}$                | 40.4               |
| CH <sub>3</sub> OH <sup>b</sup>         | 5 <sub>0</sub> – 4 <sub>0</sub> A <sup>+</sup> | 241.791                           | $6.05 \times 10^{-5}$                | 34.8               |
| CH <sub>3</sub> OH <sup>b</sup>         | 5 <sub>+1</sub> – 4 <sub>+1</sub> E            | 241.879                           | $5.96 \times 10^{-5}$                | 55.9               |
| CH <sub>3</sub> OH <sup>b</sup>         | 5 <sub>-2</sub> – 4 <sub>-2</sub> E            | 241.904                           | $5.09 \times 10^{-5}$                | 60.7               |
| S-species                               |  |                                   |                                      |                    |
| SO                                      | 5 <sub>5</sub> – 4 <sub>4</sub>                | 215.220                           | $1.20 \times 10^{-4}$                | 44                 |
| SO                                      | 6 <sub>5</sub> – 5 <sub>4</sub>                | 219.949                           | $1.35 \times 10^{-4}$                | 35                 |
| SO <sub>2</sub>                         | 4 <sub>2,2</sub> – 3 <sub>1,3</sub>            | 235.151                           | $7.69 \times 10^{-5}$                | 19                 |
| Carbon-chain species                    |  |                                   |                                      |                    |
| <i>c</i> -C <sub>3</sub> H <sub>2</sub> | 6 <sub>0,6</sub> – 5 <sub>1,5</sub>            | 217.822                           | $5.37 \times 10^{-4}$                | 39                 |
| <i>c</i> -C <sub>3</sub> H <sub>2</sub> | 5 <sub>1,4</sub> – 4 <sub>2,3</sub>            | 217.940                           | $3.98 \times 10^{-4}$                | 35                 |
| HC <sub>3</sub> N                       | 24 – 23  | 218.324                           | $8.32 \times 10^{-4}$                | 131                |

**Notes.**<sup>(a)</sup> From the Cologne Database for Molecular Spectroscopy (CDMS; Müller et al. 2001, 2005; Endres et al. 2016) and the Jet Propulsion Laboratory catalog (Pickett et al. 1998). The CH<sub>3</sub>OH transitions belonging to the CH<sub>3</sub>OH  $J_K = 5_K - 4_K$  Q-branch are also detected in the APEX data.

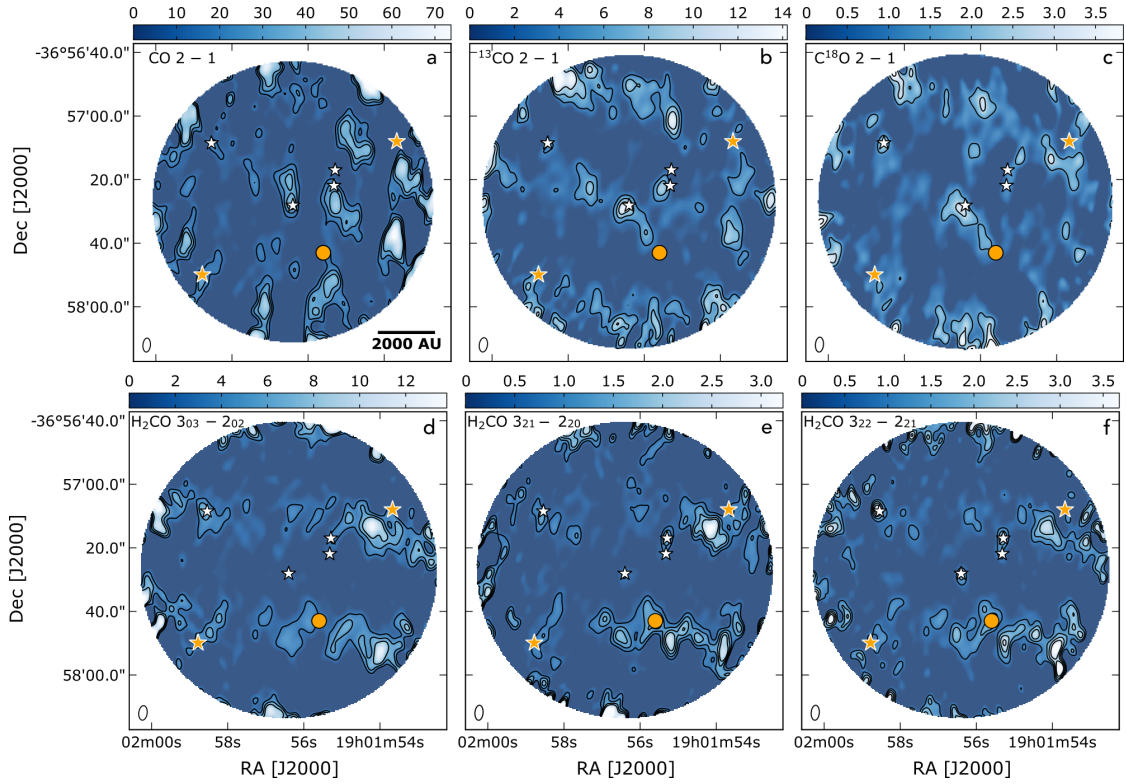


Fig. A.1: Primary beam corrected integrated intensity maps in  $\text{Jy beam}^{-1}\text{km s}^{-1}$  for the different species detected with the SMA. In each plot contours start at  $5\sigma$  and continue in intervals of  $5\sigma$ , except for panel a-c for which contours start at  $10\sigma$  and continue in intervals of  $10\sigma$ . Shown are (a) CO  $J = 2 - 1$  ( $\sigma = 0.96 \text{ Jy beam}^{-1}\text{km s}^{-1}$ ), (b)  $^{13}\text{CO}$   $J = 2 - 1$  ( $\sigma = 0.32 \text{ Jy beam}^{-1}\text{km s}^{-1}$ ), (c)  $\text{C}^{18}\text{O}$   $J = 2 - 1$  ( $\sigma = 0.13 \text{ Jy beam}^{-1}\text{km s}^{-1}$ ), (d)  $\text{H}_2\text{CO}$   $3_{03} - 2_{02}$  ( $\sigma = 0.23 \text{ mJy beam}^{-1}\text{km s}^{-1}$ ), (e)  $\text{H}_2\text{CO}$   $3_{21} - 2_{20}$  ( $\sigma = 88 \text{ mJy beam}^{-1}\text{km s}^{-1}$ ), (f)  $\text{H}_2\text{CO}$   $3_{22} - 2_{21}$  ( $\sigma = 0.14 \text{ mJy beam}^{-1}\text{km s}^{-1}$ ). The circular field-of-view corresponds to the SMA primary beam. The size of the synthesised beam is shown in the lower left corner of each image. The white and orange stars and the orange circle mark the position of the Coronet cluster members as in Fig. 1.

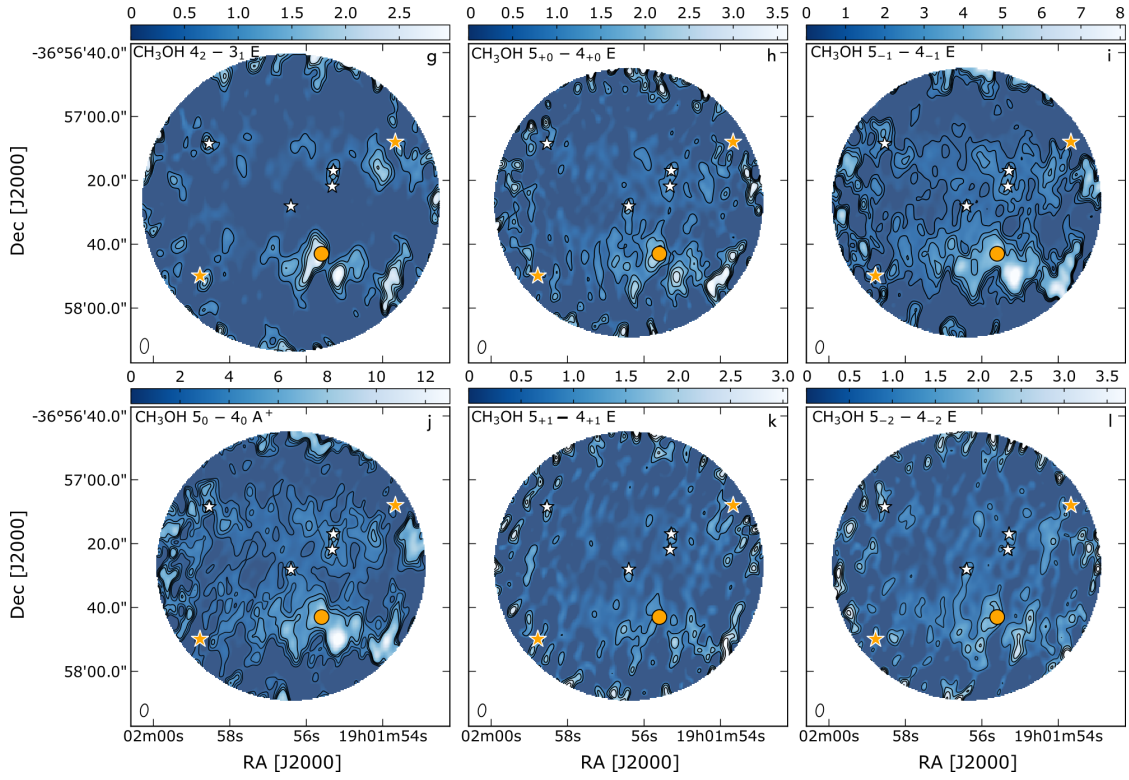


Fig. A.2: Same as Figure A.1. Primary beam corrected integrated intensity maps in  $\text{Jy beam}^{-1}\text{km s}^{-1}$  for: (g)  $\text{CH}_3\text{OH } 4_2-3_1 \text{ E}$  ( $\sigma = 88 \text{ mJy beam}^{-1}\text{km s}^{-1}$ ), (h)  $\text{CH}_3\text{OH } 5_{+0}-4_{+0} \text{ E}$  ( $\sigma = 0.12 \text{ Jy beam}^{-1}\text{km s}^{-1}$ ), (i)  $\text{CH}_3\text{OH } 5_{-1}-4_{-1} \text{ E}$  ( $\sigma = 0.13 \text{ Jy beam}^{-1}\text{km s}^{-1}$ ), (j)  $\text{CH}_3\text{OH } 5_0-4_0 \text{ A}^+$  ( $\sigma = 0.17 \text{ Jy beam}^{-1}\text{km s}^{-1}$ ), (k)  $\text{CH}_3\text{OH } 5_{+1}-4_{+1} \text{ E}$  ( $\sigma = 0.13 \text{ Jy beam}^{-1}\text{km s}^{-1}$ ), and (l)  $\text{CH}_3\text{OH } 5_{-2}-4_{-2} \text{ E}$  ( $\sigma = 0.15 \text{ mJy beam}^{-1}\text{km s}^{-1}$ ) detected by the SMA (panel g), and in the combined SMA and APEX data (panels h-l).

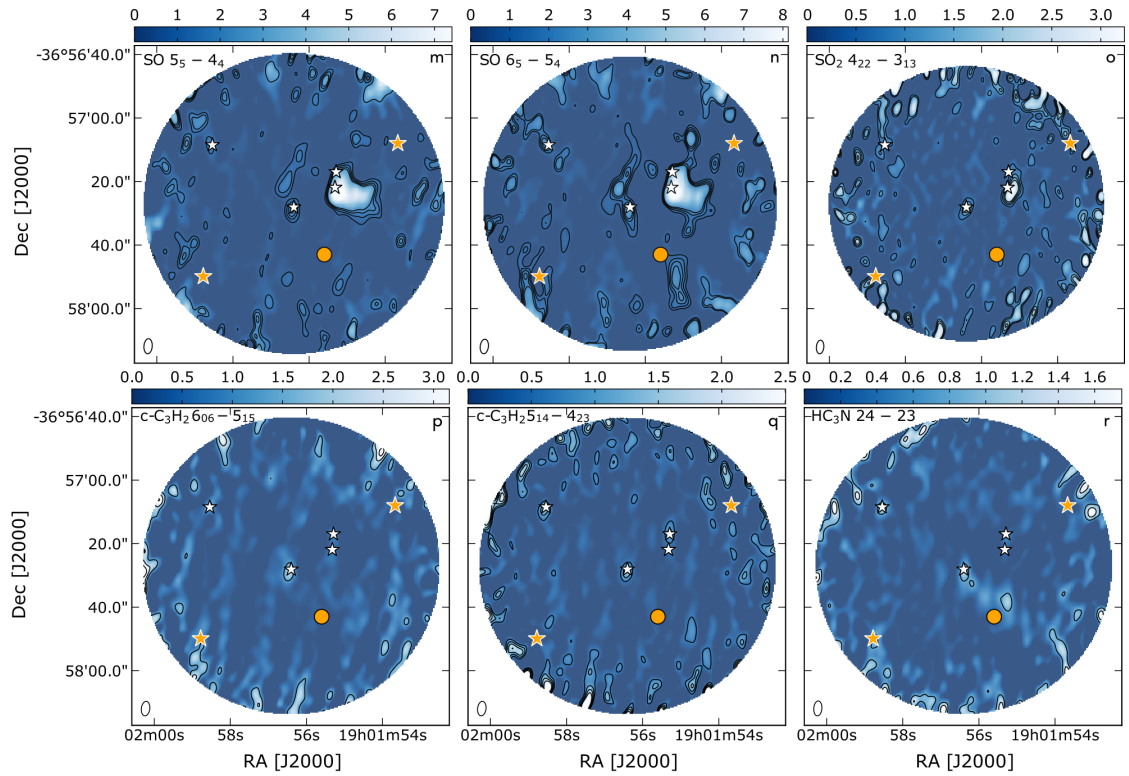


Fig. A.3: Same as Figure A.1. Primary beam corrected integrated intensity maps in  $\text{Jy beam}^{-1}\text{km s}^{-1}$  for: (m)  $\text{SO } 5_5-4_4$  ( $\sigma = 0.12 \text{ Jy beam}^{-1}\text{km s}^{-1}$ ), (n)  $\text{SO } 6_5-5_4$  ( $\sigma = 0.13 \text{ Jy beam}^{-1}\text{km s}^{-1}$ ), (o)  $\text{SO}_2 4_{22}-3_{13}$  ( $\sigma = 0.15 \text{ Jy beam}^{-1}\text{km s}^{-1}$ ), (p)  $c\text{-C}_3\text{H}_2 6_{06}-5_{15}$  ( $\sigma = 0.13 \text{ Jy beam}^{-1}\text{km s}^{-1}$ ), (q)  $c\text{-C}_3\text{H}_2 5_{14}-4_{23}$  ( $\sigma = 0.11 \text{ Jy beam}^{-1}\text{km s}^{-1}$ ), and (r)  $\text{HC}_3\text{N } J = 24-23$  ( $\sigma = 71 \text{ mJy beam}^{-1}\text{km s}^{-1}$ ) detected by the SMA.

## Appendix B: Gas-phase methanol

### Appendix B.1: Spectra of methanol

Figure B.1 shows the spectra for the brightest transitions of the CH<sub>3</sub>OH  $J_K = 5_K - 4_K$  Q-branch,  $J=5_0 - 4_0$  A<sup>+</sup> and  $J=5_{-1} - 4_{-1}$  E, respectively, extracted from the combined SMA + APEX data set. Table A.1 reports the spectral data for both CH<sub>3</sub>OH transitions. The CH<sub>3</sub>OH emission lines have a Gaussian shape and do not show blue or red-shifted components.

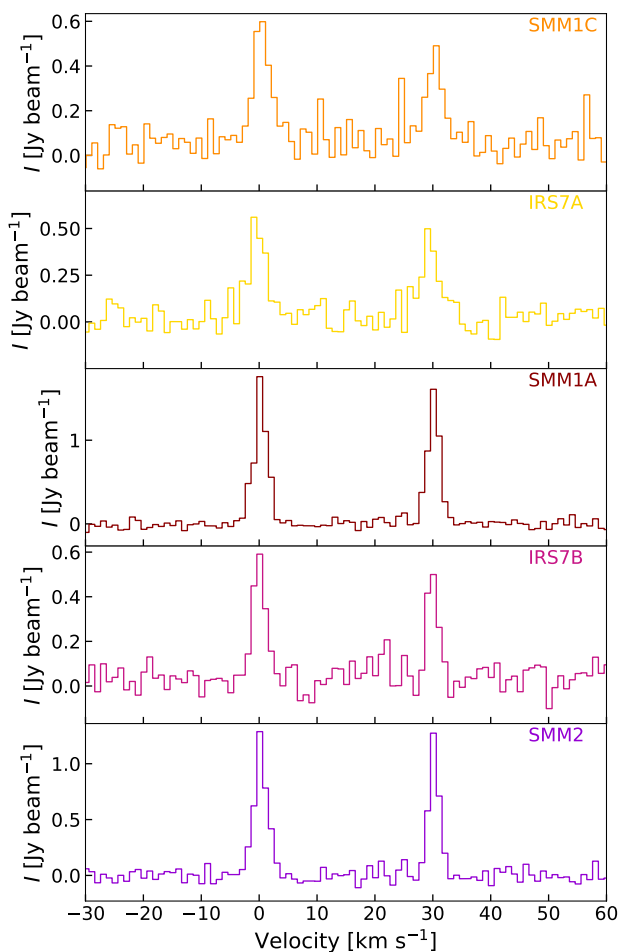


Fig. B.1: CH<sub>3</sub>OH  $J=5_0 - 4_0$  A<sup>+</sup> and CH<sub>3</sub>OH  $J=5_{-1} - 4_{-1}$  E spectra towards the Coronet cluster members detected in the combined SMA+APEX data set.

### Appendix B.2: Derivation of CH<sub>3</sub>OH column densities

The column densities of gas-phase CH<sub>3</sub>OH for the Coronet cluster members were calculated using the integrated intensities of the combined interferometric (SMA) and single-dish (APEX) data reported in Table B.1. The SMA+APEX primary beam corrected integrated intensity

(moment 0) maps for the CH<sub>3</sub>OH  $J_K = 5_K - 4_K$  Q-branch are displayed in Figure A.2.

For the column density calculation one of the two adopted procedures assumes LTE conditions, optically thin line emission, homogeneous source filling the telescope beam and a single excitation temperature to describe the level population. The equations used follow the prescription of Goldsmith & Langer (1999), but assuming a fixed rotational temperature equal to 30 K (Lindberg & Jørgensen 2012), are reported in Appendix A.4 of Perotti et al. (2021) and thus they will not be repeated here. The values used for the column densities calculation are listed in Table 2 and have been compiled from the Cologne Database for Molecular Spectroscopy (CDMS; Müller et al. 2001, 2005; Endres et al. 2016) and the Jet Propulsion Laboratory catalog (Pickett et al. 1998). In particular, the spectroscopic data are from Xu et al. (2008). The rotational diagrams for the Coronet cluster members are shown in Figure B.2. The CH<sub>3</sub>OH column densities and their uncertainties are reported in Table 3. Using a different rotational temperature (e.g., 20 K or 40 K) results in column densities being increased or decreased by approximately a factor of 0.5, respectively. The uncertainties on the gas column densities were calculated based on the spectral rms noise and on the 20% calibration uncertainty.

### Appendix B.3: Non-LTE Analysis

Further analysis of the CH<sub>3</sub>OH emission was performed using the non-LTE code RADEX (van der Tak et al. 2007). In particular, all the five CH<sub>3</sub>OH transitions were used to compare the observed relative intensities with the RADEX results for a H<sub>2</sub> number density ( $n_{\text{H}_2}$ ) in the range  $10^3 - 10^7 \text{ cm}^{-3}$  and a kinetic temperature equal to 30 K. Figure B.3 shows that all lines are in sub-thermal regime for  $n_{\text{H}_2}$  below  $10^7 \text{ cm}^{-3}$ , typical for protostellar envelopes. Figure B.4 illustrates the optical depth of the five transitions for CH<sub>3</sub>OH column densities between  $10^{13} - 10^{16} \text{ cm}^{-2}$ . The three brightest transitions ( $J = 5_{+0} - 4_{+0}$ ,  $J = 5_{-1} - 4_{-1}$ ,  $J = 5_0 - 4_0$ ) are optically thick for CH<sub>3</sub>OH column densities equal to  $10^{15} \text{ cm}^{-2}$ , while the  $J = 5_{+1} - 4_{+1}$  transition is marginally optically thick and the weakest transition,  $J = 5_{-2} - 4_{-2}$ , can be considered as optically thin. Figures B.5– B.7 show a visual comparison between CH<sub>3</sub>OH column densities calculated using RADEX and obtained from the LTE analysis for each Coronet cluster member. Thin contours represent lower limits for the integrated line intensities of the optically thick lines from Table B.1, while thick contours indicate integrated line intensities for the less optically thick lines. The thickness of these contours are given by the errors of the integrated line intensities. A range of CH<sub>3</sub>OH column densities is estimated for each source from the weakest transition (CH<sub>3</sub>OH  $J = 5_{-2} - 4_{-2}$ ) and assuming  $n_{\text{H}_2}$  between  $10^5$  and  $10^6 \text{ cm}^{-3}$  (see Table B.2). The vertical black line in Figures B.5– B.7 depicts the CH<sub>3</sub>OH column densities calculated with the LTE analysis listed in Table 3. We note that the column densities obtained with both methods are consistent for  $n_{\text{H}_2}$  equal to  $10^5 - 10^6 \text{ cm}^{-3}$  (see Table B.2).



Table B.1: Integrated CH<sub>3</sub>OH line intensities in units of Jy beam<sup>-1</sup> km s<sup>-1</sup> towards the Coronet cluster members.

| Source | $5_{+0} - 4_{+0} E^+$ | $5_{-1} - 4_{-1} E$ | $5_0 - 4_0 A^+$ | $5_{+1} - 4_{+1} E$ | $5_{-2} - 4_{-2} E$ |
|--------|-----------------------|---------------------|-----------------|---------------------|---------------------|
| SMM1C  | $1.41 \pm 0.29$       | $2.48 \pm 0.50$     | $3.86 \pm 0.77$ | $1.24 \pm 0.25$     | $1.01 \pm 0.21$     |
| IRS7A  | $0.79 \pm 0.17$       | $2.26 \pm 0.45$     | $2.94 \pm 0.59$ | $0.61 \pm 0.13$     | $0.62 \pm 0.14$     |
| SMM1A  | $2.43 \pm 0.49$       | $6.44 \pm 1.29$     | $7.23 \pm 1.45$ | $1.15 \pm 0.24$     | $2.57 \pm 0.52$     |
| IRS7B  | $1.74 \pm 0.35$       | $1.93 \pm 0.39$     | $2.97 \pm 0.60$ | $0.96 \pm 0.20$     | $1.57 \pm 0.32$     |
| SMM2   | $0.86 \pm 0.18$       | $1.97 \pm 0.40$     | $3.79 \pm 0.76$ | $0.86 \pm 0.18$     | $1.26 \pm 0.26$     |

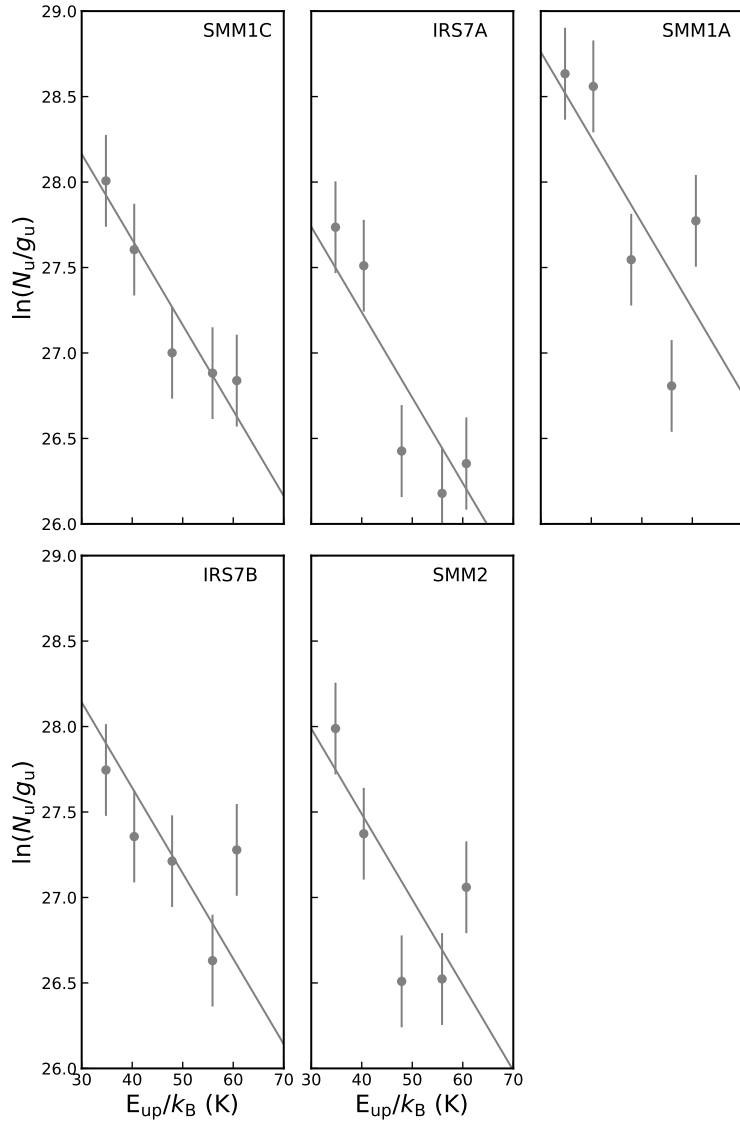


Fig. B.2: Rotational diagrams of CH<sub>3</sub>OH for the Coronet cluster members. The solid line shows the fixed slope for  $T_{\text{rot}} = 30$  K. Error bars are for  $1\sigma$  uncertainties. The column densities are reported in Table 3. Only transitions belonging to the  $J = 5_K - 4_K$  Q-branch have been considered.

Table B.2: Comparison between total CH<sub>3</sub>OH gas column densities ( $N$ ) calculated using the LTE and the non-LTE analyses towards the Coronet cluster members.

| Object | $N_{\text{CH}_3\text{OH}}^{\text{gas, LTE}} (a)$<br>[ $10^{15}\text{cm}^{-2}$ ] | $N_{\text{CH}_3\text{OH}}^{\text{gas, non-LTE}} (b)$<br>[ $10^{15}\text{cm}^{-2}$ ] |
|--------|---|---|
| SMM1C  | $1.95 \pm 0.23$   | 1.03 – 5.50   |
| IRS7A  | $1.28 \pm 0.15$   | 0.94 – 3.50   |
| SMM1A  | $3.54 \pm 0.43$   | 1.50 – 10.0   |
| IRS7B  | $1.91 \pm 0.23$   | 1.07 – 7.30   |
| SMM2   | $1.64 \pm 0.20$   | 1.04 – 6.30   |

**Notes.** (a) CH<sub>3</sub>OH column densities calculated with the LTE analysis and fixing  $T_{\text{rot}} = 30$  K. (b) CH<sub>3</sub>OH column densities determined using the non-LTE code RADEX for  $T_{\text{kin}} = 30$  K and  $n_{\text{H}_2} = 10^5 - 10^6 \text{cm}^{-3}$ .

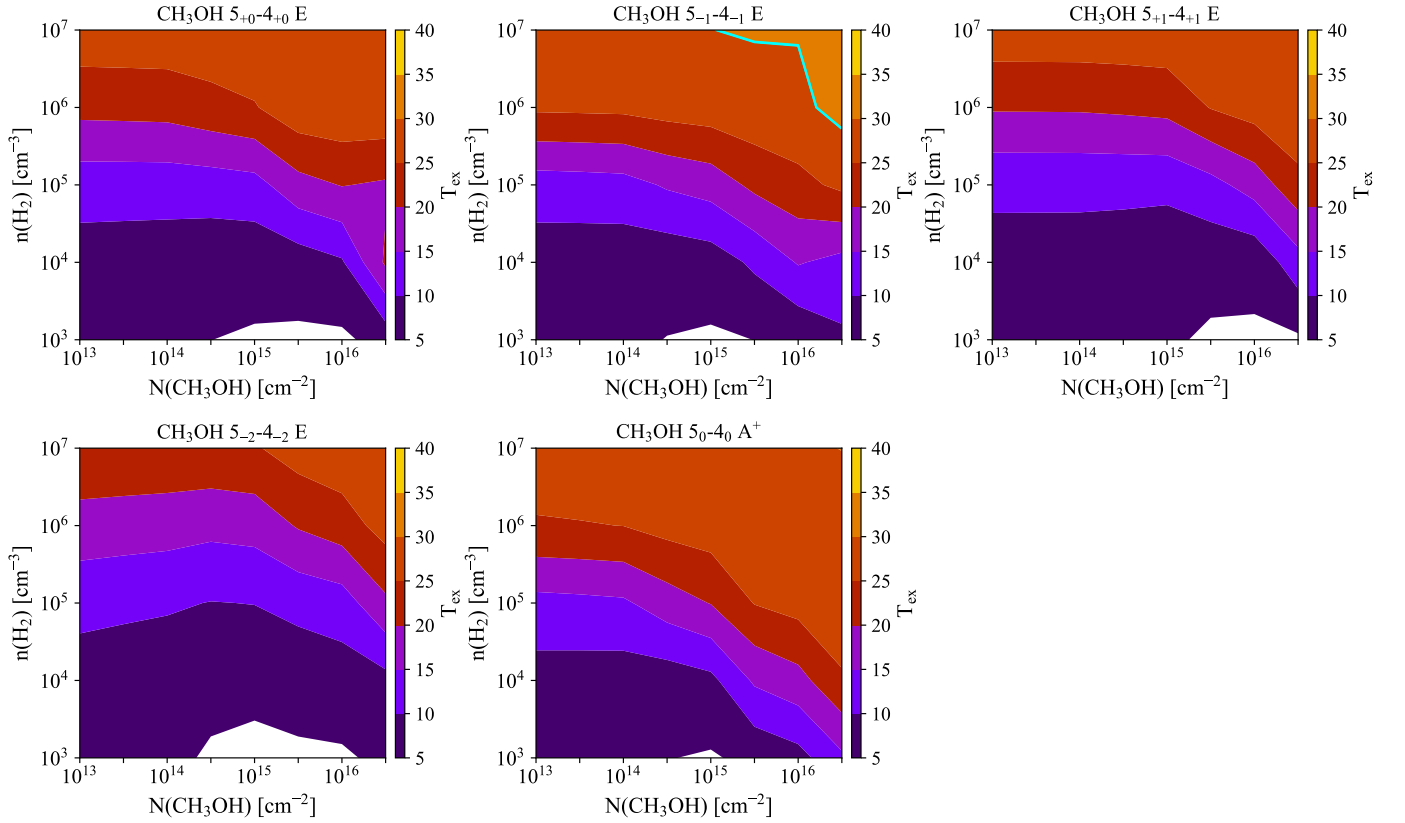


Fig. B.3: RADEX model results for the five CH<sub>3</sub>OH transitions (Table A.1) using  $T_{\text{kin}} = 30$  K. The cyan line indicates  $T_{\text{ex}} = 30$  K.

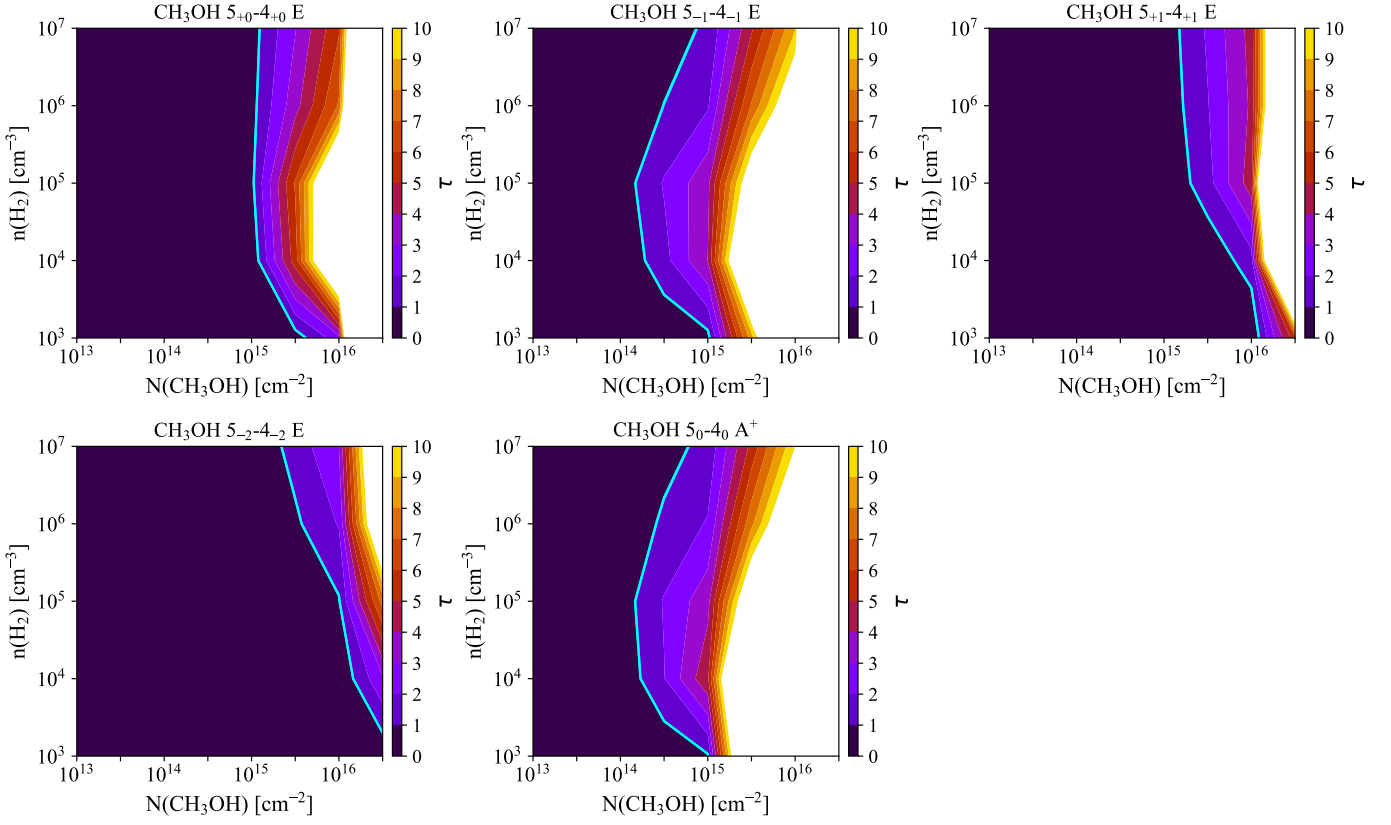


Fig. B.4: Optical depth for the five CH<sub>3</sub>OH transitions obtained with RADEX, using  $T_{\text{kin}} = 30$  K. The cyan line represents  $\tau = 1$ .

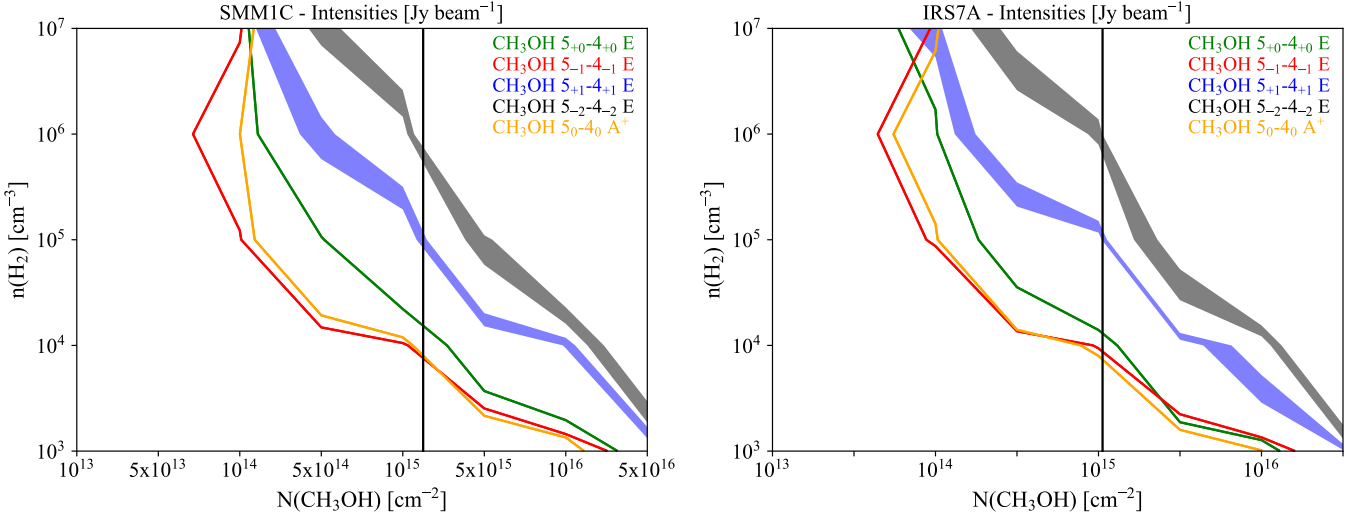


Fig. B.5: RADEX model results for the observed CH<sub>3</sub>OH lines towards SMM1C (left) and IRS7A (right), using  $T_{\text{kin}} = 30$  K. Red, orange and green contours represent lower limits for the integrated line intensities of optically thick lines whereas blue and gray contours represent the marginally optically thin lines and include the errors from Table B.1. The vertical line is the CH<sub>3</sub>OH column density calculated assuming LTE conditions and optically thin emission reported in Table 3.

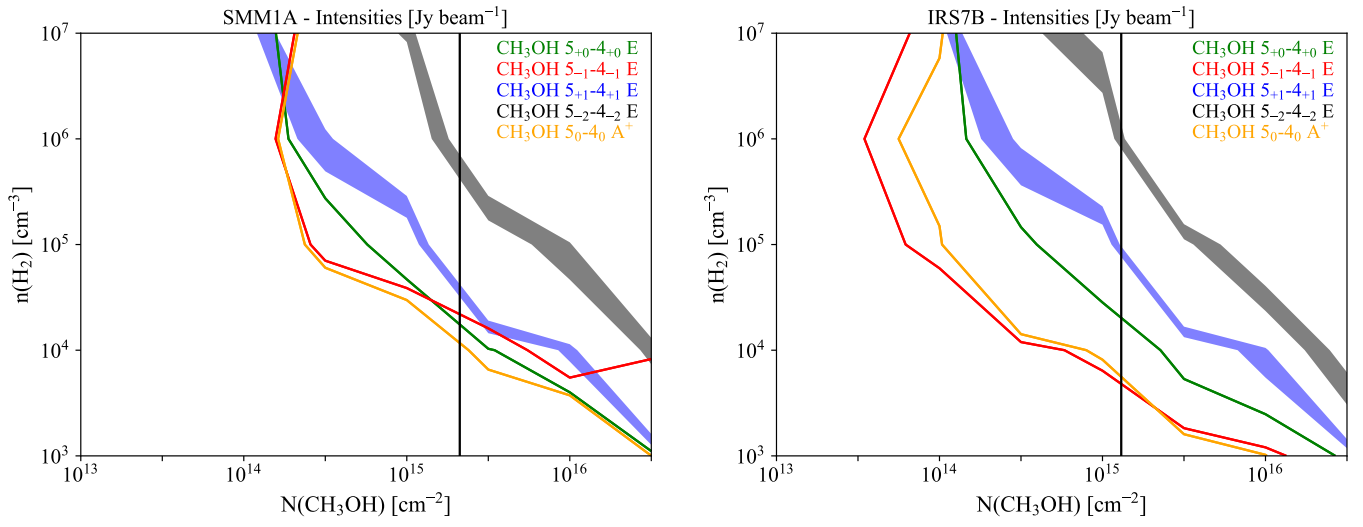


Fig. B.6: Same as Figure B.5 for SMM1A (left) and IRS7B (right).

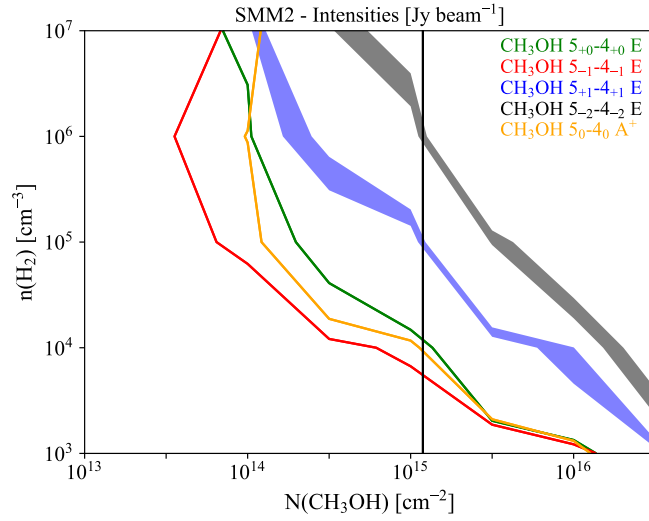


Fig. B.7: Same as Figure B.5 for SMM2.